

Walk-on-Interfaces: A Monte Carlo Estimator for an Elliptic Interface Problem with Nonhomogeneous Flux Jump Conditions and a Neumann Boundary Condition

Xinwen Ding, Adam R Stinchcombe

August 26, 2025

Contents

1	Introduction	3
2	Summary of the Walk-on-Boundary Method	6
3	Boundary Integral Formulation	8
4	The Walk-on-Interfaces Method	11
4.1	A Theorem Towards Walk-on-Interfaces (WoI) Estimator	12
4.2	Naive Walk-on-Interfaces	12
4.2.1	Transitional Probability Function	13
4.2.2	The Naive WoI Estimator	13
4.2.3	Sampling Strategy	14
4.2.4	Reuse of Markov Chains	16
4.3	Acceleration	17
4.3.1	The WoI Estimator	17
4.3.2	A Summary of the WoI Procedure	18
4.4	Variance Reduction	20
4.5	Gradient Estimation	21
4.6	Implementation Considerations	23

5	Results	25
6	Conclusion	40
	References	42
A	A Proof of Theorem 4.1	46
B	A Proof of Theorem 4.2	48

Abstract

Elliptic interface problems arise in numerous scientific and engineering applications, modeling heterogeneous materials in which physical properties change discontinuously across interfaces. In this paper, we present *Walk-on-Interfaces* (WoI), a grid-free Monte Carlo estimator for a class of Neumann elliptic interface problems with nonhomogeneous flux jump conditions. Our Monte Carlo estimators maintain consistent accuracy throughout the domain and, thus, do not suffer from the well-known close-to-source evaluation issue near the interfaces. We also presented a simple modification with reduced variance. Estimation of the gradient of the solution can be performed, with almost no additional cost, by simply computing the gradient of the Green’s function in WoI. Taking a scientific machine learning approach, we use our estimators to provide training data for a deep neural network that outputs a continuous representation of the solution. This regularizes our solution estimates by removing the high-frequency Monte Carlo error. All of our estimators are highly parallelizable, have a $\mathcal{O}(1/\sqrt{W})$ convergence rate in the number of samples, and generalize naturally to higher dimensions. We solve problems with many interfaces that have irregular geometry and in up to dimension six. Numerical experiments demonstrate the effectiveness of the approach and to highlight its potential in solving problems motivated by real-world applications.

1 Introduction

Elliptic interface problems arise in a wide range of scientific and engineering applications, from electrostatics of biomolecules [15] and tissues with packed cells [44], to porous media flow [28, 37], geophysics [34], and composite materials [42]. Elliptic interface problems are often the forward problem in important inverse problems. In particular, electrical impedance tomography [40] and electroencephalography [41] can be formulated as such an inverse problem.

Mathematically, interface problems are characterized by partial differential equations (PDEs) with spatially varying coefficients that are discontinuous across interfaces, reflecting sudden changes in physical properties. The canonical elliptic PDE is

$$\nabla \cdot (\sigma(\mathbf{x}) \nabla u(\mathbf{x})) = 0, \quad \mathbf{x} \in \Omega. \quad (1)$$

We assume that $\sigma(\mathbf{x}) \geq 0$ is piecewise constant. The boundaries between the regions of constant σ give rise to interfaces. Since $\sigma(\mathbf{x})$ is not differentiable across these interfaces, it is common to derive interface conditions consistent with Eq. (1).

To organize the regions of constant σ , we employ a tree definition of domains with subregions that have different physical properties separated by interfaces. Consider a bounded, simply connected domain $\Omega \subseteq \mathbb{R}^m$ with a smooth boundary, $\partial\Omega$. Let $N < \infty$ be the total number of non-overlapping regions inside Ω . For each $i \in \{1, \dots, N\}$, we denote the i^{th} region and all its descendants as $\Omega_i \subseteq \Omega$, and we require the interface $\partial\Omega_i \in \mathcal{C}^2$. The tree definition from [19], where $\partial\Omega_1 = \partial\Omega$, is adopted here to describe the hierarchical relationships among the regions. An example of a domain layout and its associated tree definition is provided in Figure 1.

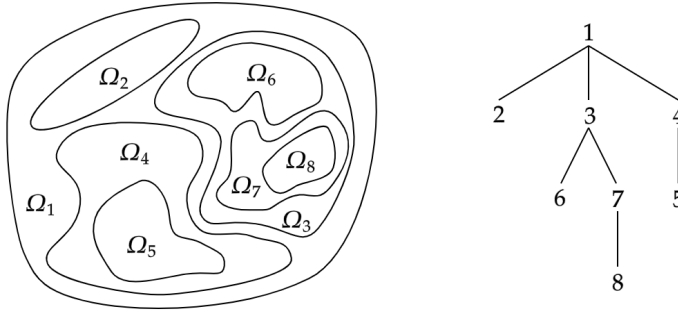


Figure 1: An example of tree-structured domain defined by [19]. The outer boundary of the root region of the tree, Ω_1 , is also the boundary of the domain. Each interface is shared between a region and its unique parent.

Let $\mathbf{n}(\mathbf{x})$ denote the unit outward normal on the boundary. Correspondingly, we denote $\partial_{\mathbf{n}}$ or $\frac{\partial}{\partial \mathbf{n}}$ as the normal derivative. We further define the jump of a function $f : \partial\Omega_i \rightarrow \mathbb{R}$ across some interface $\partial\Omega_i$ at some point \mathbf{x}_0 by

$$[f(\mathbf{x}_0)] := f_+(\mathbf{x}_0) - f_-(\mathbf{x}_0),$$

where $f_+(\mathbf{x}_0)$ is the limit point of $f(\mathbf{x})$ as $\mathbf{x} \rightarrow \mathbf{x}_0$ from the exterior of Ω_i (i.e. from $\Omega \setminus \Omega_i$), while $f_-(\mathbf{x}_0)$ is the limit point of $f(\mathbf{x})$ as $\mathbf{x} \rightarrow \mathbf{x}_0$ from the interior of Ω_i (i.e. from Ω_i).

Under the assumption that $\sigma(\mathbf{x})$ is piecewise constant, the PDE Eq. (1) can be cast into the interface problem with Neumann boundary condition,

$$\begin{cases} \Delta u(\mathbf{x}) = 0 & \text{in } \Omega \setminus \cup_i \partial\Omega_i & (2a) \\ \sigma_1 \partial_{\mathbf{n}} u(\mathbf{x}) = b_1(\mathbf{x}) & \text{on } \partial\Omega_1 & (2b) \\ [u](\mathbf{x}) = 0 & \text{on } \partial\Omega_i, \forall i \in \{2, 3, \dots, N\} & (2c) \\ [\sigma \partial_{\mathbf{n}} u](\mathbf{x}) = b_i(\mathbf{x}) & \text{on } \partial\Omega_i, \forall i \in \{2, 3, \dots, N\}, & (2d) \end{cases}$$

where $b_i \in \mathcal{C}^{0,1}$ and $\sigma(\mathbf{x})|_{\Omega_i} \equiv \sigma_i$ for each $i = 1, 2, \dots, N$. For the i^{th} region, we let p_i denote the index of its unique parent in the tree definition of the domain. Then, $\sigma(\mathbf{x})$ jumps across $\partial\Omega_i$ from σ_i to σ_{p_i} . We additionally require $\int_{\partial\Omega_i} b_i(\mathbf{x}) dA = 0, \forall i \in \{1, \dots, N\}$ to ensure the well-posedness of the interface problem, up to an additive constant [7].

Classical numerical methods for solving elliptic interface problems have been extensively studied over the past several decades. These numerical methods typically require a high-quality underlying mesh to define the boundary and the interface. Methods that explicitly compute discretized derivatives, such as the finite element method [39, 11], the finite difference method [22, 23, 8], and the finite volume method [6], often lead to a large and ill-conditioned linear system. Integral equation methods, such as the boundary element method [5] and the boundary integral equation method [44], result in well-conditioned dense linear systems after discretization. The linear systems can be solved rapidly when coupled with the fast multiple method [10, 25]. One well-known challenge for integral equation methods is accurately evaluating a nearly singular kernel at points close to the interface, which is usually tackled by carefully designed quadratures [14, 16]. Another common challenge is handling domains that contain a large number (often close-to-touching) of interfaces [1].

Monte Carlo methods are a powerful class of grid-free computational tools that estimate solutions to PDEs through random sampling. There are two major types of algorithms in the Monte Carlo family, *Walk-on-Sphere* (WoS) and *Walk-on-Boundary* (WoB). WoS [27] was first proposed to solve Laplace equations by simulating the paths of Brownian motion. Later, it was generalized to other problems [3, 20, 36], and more complex domain geometries [35, 21, 26]. Algorithms in the class of WoS rely on an ϵ -shell near the boundary to stop the Brownian motion, which results in inaccurate estimation near the boundary. The WoB methods, rooted in potential theory, do not suffer from this limitation. It was first introduced to solve the Lamé equation [30]. Later, WoB was extended to solve Laplace and Poisson problems with Dirichlet, Neumann, and Robin boundary conditions [32, 31, 33]. One recent work [38] summarized existing WoB estimators, proposed a new WoB estimator for the Neumann problem, and emphasized particular applications of WoB in computer graphics.

In this paper, we present *Walk-on-Interfaces* (WoI), an extension of the family of WoB methods designed to solve the Neumann elliptic interface problem with nonhomogeneous flux jump conditions in Eq. (2) with $N \geq 1$. To the best of our knowledge, this is the first Monte Carlo estimator for an interface problem.

The proposed Monte Carlo estimators offer several important advantages. They

are grid-free, highly parallelizable, and can be easily generalized to solve high-dimensional problems. Our estimators maintain consistent accuracy near and even on the boundary and the interfaces, as well as in the interior of the domain. By computing the gradient of our Monte Carlo estimators, we obtain an estimation to the gradient of the solution to the interface problem almost without extra cost. The estimators and their associated gradient estimators have $\mathcal{O}(1/\sqrt{W})$ convergence rate in the number of samples W .

As an application, these estimators can be combined with a neural network to form a WoI framework, in which the estimators play the role of data generators. The output of this framework provides a continuous approximation of the solution to the interface problem, free from high-frequency Monte Carlo error. This data-driven approach is especially beneficial in domains with multiple interfaces.

The rest of this paper is organized as follows: In Section 2, we review and summarize the WoB estimator for the interior Neumann problem. In section 3, we present the boundary integral formulation for the elliptic interface problem, which is foundational for the WoI estimator. Building on this, we present the WoI estimator and its variance-reduced counterpart in Section 4. Then, in Section 5, we investigate the performance of our estimators and the WoI framework via both synthetic examples with known ground truth and examples motivated by real-world applications. Finally, we conclude this paper and discuss possible directions for future work in Section 6.

2 Summary of the Walk-on-Boundary Method

In this section, we provide a brief summary of the WoB method [32] for the interior Neumann problem for the Laplace equation,

$$\begin{cases} \Delta v(\mathbf{x}) = 0, & \mathbf{x} \in \Omega \\ \frac{\partial v}{\partial \mathbf{n}(\mathbf{x})} = g(\mathbf{x}), & \mathbf{x} \text{ on } \partial\Omega \end{cases}. \quad (3)$$

The Neumann boundary data g must satisfy the solvability condition,

$$\int_{\partial\Omega} g(\mathbf{x}) \, dA = 0.$$

It is well-known that the solution to Eq. (3) is unique up to a constant [7]. The WoB estimator estimates one particular solution, while the full family of solutions is obtained by shifting the particular solution according to a selected reference point.

The estimator relies on the fact that solutions, up to an additive constant, to the interior Neumann problem can be represented with a single-layer potential,

$$v(\mathbf{x}) = \int_{\partial\Omega} \Phi(\mathbf{x}, \mathbf{y}) \gamma^*(\mathbf{y}) dA_{\mathbf{y}}, \quad \forall \mathbf{x} \in \Omega,$$

in which

$$\Phi(\mathbf{x}, \mathbf{y}) = \begin{cases} -\frac{1}{2\pi} \ln |\mathbf{x} - \mathbf{y}| & d = 2 \\ \frac{1}{d(d-2)\alpha(d)} \frac{1}{|\mathbf{x} - \mathbf{y}|^{d-2}} & d \geq 3 \end{cases}$$

is the Green's function, $\alpha(d) = \frac{\pi^{d/2}}{\Gamma(\frac{d}{2}+1)}$ is the volume of the unit ball in \mathbb{R}^d , and $\gamma^*(\mathbf{y})$ is a continuous density on the boundary $\partial\Omega$. Let us denote

$$K^*(\mathbf{x}, \mathbf{y}) := -\frac{\partial \Phi(\mathbf{x}, \mathbf{y})}{\partial \mathbf{n}(\mathbf{x})} = \frac{1}{d\alpha(d)} \frac{(\mathbf{x} - \mathbf{y}) \cdot \mathbf{n}(\mathbf{x})}{|\mathbf{x} - \mathbf{y}|^d}.$$

Let $\{Y_0, Y_1, \dots, Y_i \dots\}$ be a Markov chain with transitional probability density functions (PDFs),

$$p(\mathbf{x}, \mathbf{y}_0) = \frac{1}{|\partial\Omega|} \quad \text{and} \quad p(\mathbf{y}_{i-1}, \mathbf{y}_i) = \frac{2}{d\alpha(d)} \frac{|(\mathbf{y}_i - \mathbf{y}_{i-1}) \cdot \mathbf{n}(\mathbf{y}_i)|}{q(\mathbf{y}_{i-1}, \mathbf{y}_i) |\mathbf{y}_i - \mathbf{y}_{i-1}|^m},$$

such that \mathbf{y}_i is a realization of the state Y_i , and that $q(\mathbf{y}_{i-1}, \mathbf{y}_i)$ is the number of intersections, distinct from \mathbf{y}_{i-1} , between Ω and a line,

$$\ell(t) = t\mathbf{d} + \mathbf{y}_{i-1},$$

whose direction \mathbf{d} is uniformly randomly selected in \mathbb{R}^d . The WoB estimator is

$$v(\mathbf{x}) \approx \mathbb{E}_{Y_i} \left[2 \sum_{i=0}^{M-1} 2^i T_i Q_i \Phi(\mathbf{x}, Y_i) + 2^M T_M Q_M \Phi(\mathbf{x}, Y_M) \right], \quad (4)$$

in which

$$Q_i = \begin{cases} \frac{g(Y_0)}{p(\mathbf{x}, Y_0)} & \text{if } i = 0 \\ Q_{i-1} \frac{K^*(Y_i, Y_{i-1})}{p(Y_{i-1}, Y_i)} = \frac{1}{2} Q_{i-1} & \text{if } i \geq 1 \end{cases}, \quad (5)$$

and

$$T_i = \begin{cases} 1 & \text{if } i = 0 \\ \prod_{m=1}^i q(Y_{m-1}, Y_m) \text{sign}[(Y_m - Y_{m-1}) \cdot \mathbf{n}(Y_m)] & \text{if } i \geq 1 \end{cases}. \quad (6)$$

We provide concrete examples in Figure 2 to visualize WoB trajectories. The Markov chain moves around the boundary by finding the intersections between the boundary and lines in uniformly random directions. For nonconvex domains, where multiple intersections may occur, one is selected uniformly at random.

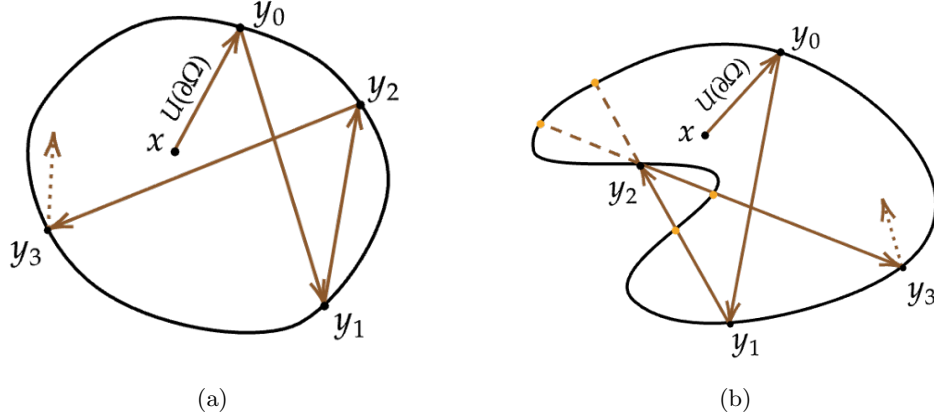


Figure 2: A example diagram of the WoB method in a $d = 2$ domain. (a) One possible WoB trajectory with a convex domain with $M = 3$. Notice that when Ω is convex, $q(\mathbf{y}_{i-1}, \mathbf{y}_i) = 1$ always holds when $\ell(t)$ is not in the tangent plane. (b) One possible WoB trajectory with a general domain with $M = 3$. In both situations, \mathbf{y}_0 is sampled uniformly on $\partial\Omega$, annotated by $U(\partial\Omega)$ alongside the arrow from \mathbf{x} to \mathbf{y}_0 . For all other arrows without annotations, \mathbf{y}_i 's are determined by finding an intersection of $\partial\Omega$ and a ray with random direction with origin \mathbf{y}_{i-1} .

3 Boundary Integral Formulation

As the first step towards our *Walk-on-Interfaces* estimator, we present the boundary integral formulation for the elliptic interface problem. This formulation is based on the work in a recent thesis by Kyle Waller Bower [19].

Given a query point $\mathbf{x} \in \Omega$, the solution $u(\mathbf{x})$ of the elliptic interface problem can be represented as the sum of N single-layer potentials,

$$u(\mathbf{x}) = \sum_{j=1}^N \mathcal{S}_{\partial\Omega_j}[\gamma_j^*](\mathbf{x}) = \sum_{j=1}^N \int_{\partial\Omega_j} \Phi(\mathbf{x}, \mathbf{y}) \gamma_j^*(\mathbf{y}) dA_{\mathbf{y}},$$

in which $\Phi(\mathbf{x}, \mathbf{y})$ is the Green's function, and $\gamma_j^* \in \mathcal{C}(\partial\Omega_j)$ is the charge density function on $\partial\Omega_j$. Furthermore, since we assumed the interfaces do not overlap with each other, the solution is then

$$u(\mathbf{x}) = \int_{\Gamma} \Phi(\mathbf{x}, \mathbf{y}) \left(\sum_{j=1}^N \gamma_j^*(\mathbf{y}) \mathbb{1}_{\partial\Omega_j} \right) dA_{\mathbf{y}}, \quad (7)$$

in which $\Gamma = \bigsqcup_{j=1}^N \partial\Omega_j$ is the *disjoint* union of the boundary and all of the interfaces.

We need to solve for the charge densities, $\gamma_j^*(\mathbf{y})$, to solve for $u(\mathbf{x})$. A classic theorem in potential theory [18] characterizes the jump of $\frac{\partial \mathcal{S}_{\partial\Omega_j}[\gamma_j^*](\mathbf{x})}{\partial \mathbf{n}(\mathbf{x})}$ across the

interface,

$$\left(\frac{\partial \mathcal{S}_{\partial\Omega_j}[\gamma_j^*](\mathbf{x})}{\partial \mathbf{n}(\mathbf{x})} \right)_{\pm} = \mp \frac{1}{2} \gamma_j^*(\mathbf{x}) \delta_{ij} + \int_{\partial\Omega_j} \frac{\partial \Phi(\mathbf{x}, \mathbf{y})}{\partial \mathbf{n}(\mathbf{x})} \gamma_j^*(\mathbf{y}) dA_{\mathbf{y}}, \quad \forall \mathbf{x} \in \partial\Omega_j, \quad (8)$$

in which δ_{ij} is the Kronecker-delta function, and the subscript $+$ (or $-$) on the left-hand-side denotes the outward (or inward) normal direction.

We introduce the following notation that encodes the location of \mathbf{x} and \mathbf{y} using subscript indices i and j . In particular,

$$K_{i,j}^*(\mathbf{x}, \mathbf{y}) := -\frac{\partial \Phi(\mathbf{x}, \mathbf{y})}{\partial \mathbf{n}(\mathbf{x})} = \frac{1}{d\alpha(d)} \frac{(\mathbf{x} - \mathbf{y}) \cdot \mathbf{n}(\mathbf{x})}{|\mathbf{x} - \mathbf{y}|^d}, \quad \text{for } \mathbf{x} \in \partial\Omega_i, \mathbf{y} \in \partial\Omega_j,$$

in which d is the dimension of the problem, and $\alpha(d) = \frac{\pi^{d/2}}{\Gamma(\frac{d}{2}+1)}$ is the volume of the unit ball in \mathbb{R}^d . Correspondingly, we define an integral operator $\mathcal{K}_{i,j}^*$ such that

$$\mathcal{K}_{i,j}^* \gamma_j^* = \int_{\partial\Omega_j} K_{i,j}^*(\mathbf{x}, \mathbf{y}) \gamma_j^*(\mathbf{y}) dA_{\mathbf{y}}.$$

Imposing the boundary condition (2b) and the interface condition (2d) using Eq. (8) yields a system of N integral equations, one for each charge density function $\gamma_i^*, \forall i \in \{1, \dots, N\}$,

$$\left\{ \begin{array}{l} \frac{1}{2} \sigma_1 \gamma_1^*(\mathbf{x}) - \sigma_1 \sum_{j=1}^N \mathcal{K}_{1,j}^* \gamma_j^* = b_1(\mathbf{x}), \quad \mathbf{x} \in \partial\Omega_1 \end{array} \right. \quad (9a)$$

$$\left\{ \begin{array}{l} -\frac{1}{2} (\sigma_{p_i} + \sigma_i) \gamma_i^*(\mathbf{x}) - (\sigma_{p_i} - \sigma_i) \sum_{j=1}^N \mathcal{K}_{i,j}^* \gamma_j^* = b_i(\mathbf{x}), \quad \mathbf{x} \in \partial\Omega_i, \\ \text{for } i = 2, 3, \dots, N, \end{array} \right. \quad (9b)$$

in which the region indexed by $p_i \in \{1, 2, \dots, N\}$ is the parent of region i , under the tree-structure definition of the domain. Rearranging the system so that the coefficients in front of γ_i^* are equal to 1, we obtain

$$\gamma_i^*(\mathbf{x}) - \alpha_i \sum_{j=1}^N \mathcal{K}_{i,j}^* \gamma_j^* = \beta_i(\mathbf{x}), \quad \mathbf{x} \in \partial\Omega_i, \text{ for } i = 1, \dots, N, \quad (10)$$

in which $\alpha_i = \begin{cases} 2 & \text{if } i = 1 \\ \frac{2(\sigma_i - \sigma_{p_i})}{\sigma_{p_i} + \sigma_i} & \text{if } i = 2, 3, \dots, N \end{cases}$ are constants, and $\beta_i : \partial\Omega_i \rightarrow \mathbb{R}$ are

functions defined as $\beta_i(\mathbf{x}) = \begin{cases} \frac{2}{\sigma_1} b_1(\mathbf{x}) & \text{if } i = 1 \\ -\frac{2}{\sigma_{p_i} + \sigma_i} b_i(\mathbf{x}) & \text{if } i = 2, 3, \dots, N. \end{cases}$

We can write Eq. (10) in matrix form,

$$(I_{N \times N} - \mathcal{M})\gamma^* = \beta, \quad (11)$$

where

$$\mathcal{M} = \begin{bmatrix} \alpha_1 \mathcal{K}_{1,1}^* & \alpha_1 \mathcal{K}_{1,2}^* & \cdots & \alpha_1 \mathcal{K}_{1,N}^* \\ \alpha_2 \mathcal{K}_{2,1}^* & \alpha_2 \mathcal{K}_{2,2}^* & \cdots & \alpha_2 \mathcal{K}_{2,N}^* \\ \vdots & \vdots & \ddots & \vdots \\ \alpha_N \mathcal{K}_{N,1}^* & \alpha_N \mathcal{K}_{N,2}^* & \cdots & \alpha_N \mathcal{K}_{N,N}^* \end{bmatrix}, \quad \gamma^* = \begin{bmatrix} \gamma_1^* \\ \gamma_2^* \\ \vdots \\ \gamma_N^* \end{bmatrix}, \quad \text{and } \beta = \begin{bmatrix} \beta_1 \\ \beta_2 \\ \vdots \\ \beta_N \end{bmatrix}.$$

We can express the solution to Eq. (11) as a Neumann series,

$$\gamma^* = \sum_{i=0}^{\infty} \mathcal{M}^i \beta \quad (12)$$

$$\begin{aligned} &= \begin{bmatrix} \beta_1 + \sum_{h_0=1}^N (\alpha_1 \mathcal{K}_{1,h_0}^*) \beta_{h_0} + \sum_{h_1=1}^N \sum_{h_0=1}^N (\alpha_1 \mathcal{K}_{1,h_1}^*) (\alpha_{h_1} \mathcal{K}_{h_1,h_0}^*) \beta_{h_0} + \cdots \\ \beta_2 + \sum_{h_0=1}^N (\alpha_2 \mathcal{K}_{2,h_0}^*) \beta_{h_0} + \sum_{h_1=1}^N \sum_{h_0=1}^N (\alpha_2 \mathcal{K}_{2,h_1}^*) (\alpha_{h_1} \mathcal{K}_{h_1,h_0}^*) \beta_{h_0} + \cdots \\ \vdots \\ \beta_N + \sum_{h_0=1}^N (\alpha_N \mathcal{K}_{N,h_0}^*) \beta_{h_0} + \sum_{h_1=1}^N \sum_{h_0=1}^N (\alpha_N \mathcal{K}_{N,h_1}^*) (\alpha_{h_1} \mathcal{K}_{h_1,h_0}^*) \beta_{h_0} + \cdots \end{bmatrix} \\ &= \begin{bmatrix} \beta_1 \\ \beta_2 \\ \vdots \\ \beta_N \end{bmatrix} + \sum_{i=1}^{\infty} \begin{bmatrix} \sum_{h_{i-1}=1}^N \cdots \sum_{h_1=1}^N \sum_{h_0=1}^N (\alpha_1 \mathcal{K}_{1,h_{i-1}}^*) \cdots (\alpha_{h_2} \mathcal{K}_{h_2,h_1}^*) (\alpha_{h_1} \mathcal{K}_{h_1,h_0}^*) \beta_{h_0} \\ \sum_{h_{i-1}=1}^N \cdots \sum_{h_1=1}^N \sum_{h_0=1}^N (\alpha_2 \mathcal{K}_{2,h_{i-1}}^*) \cdots (\alpha_{h_2} \mathcal{K}_{h_2,h_1}^*) (\alpha_{h_1} \mathcal{K}_{h_1,h_0}^*) \beta_{h_0} \\ \vdots \\ \sum_{h_{i-1}=1}^N \cdots \sum_{h_1=1}^N \sum_{h_0=1}^N (\alpha_N \mathcal{K}_{N,h_{i-1}}^*) \cdots (\alpha_{h_2} \mathcal{K}_{h_2,h_1}^*) (\alpha_{h_1} \mathcal{K}_{h_1,h_0}^*) \beta_{h_0} \end{bmatrix}. \end{aligned} \quad (13)$$

As for the WoB estimator, we obtain a finite-term approximation of γ^* using a

truncation method [32] as in the WoB estimator. For some fixed $0 \leq M < \infty$,

$$\begin{aligned} \boldsymbol{\gamma}^* \approx & \begin{bmatrix} \beta_1 \\ \beta_2 \\ \vdots \\ \beta_N \end{bmatrix} + \sum_{i=1}^{M-1} \begin{bmatrix} \sum_{h_{i-1}=1}^N \cdots \sum_{h_1=1}^N \sum_{h_0=1}^N (\alpha_1 \mathcal{K}_{1,h_{i-1}}^*) \cdots (\alpha_{h_2} \mathcal{K}_{h_2,h_1}^*) (\alpha_{h_1} \mathcal{K}_{h_1,h_0}^*) \beta_{h_0} \\ \sum_{h_{i-1}=1}^N \cdots \sum_{h_1=1}^N \sum_{h_0=1}^N (\alpha_2 \mathcal{K}_{2,h_{i-1}}^*) \cdots (\alpha_{h_2} \mathcal{K}_{h_2,h_1}^*) (\alpha_{h_1} \mathcal{K}_{h_1,h_0}^*) \beta_{h_0} \\ \vdots \\ \sum_{h_{i-1}=1}^N \cdots \sum_{h_1=1}^N \sum_{h_0=1}^N (\alpha_N \mathcal{K}_{N,h_{i-1}}^*) \cdots (\alpha_{h_2} \mathcal{K}_{h_2,h_1}^*) (\alpha_{h_1} \mathcal{K}_{h_1,h_0}^*) \beta_{h_0} \end{bmatrix} \\ & + \frac{1}{2} \begin{bmatrix} \sum_{h_{M-1}=1}^N \cdots \sum_{h_1=1}^N \sum_{h_0=1}^N (\alpha_1 \mathcal{K}_{1,h_{M-1}}^*) \cdots (\alpha_{h_2} \mathcal{K}_{h_2,h_1}^*) (\alpha_{h_1} \mathcal{K}_{h_1,h_0}^*) \beta_{h_0} \\ \sum_{h_{M-1}=1}^N \cdots \sum_{h_1=1}^N \sum_{h_0=1}^N (\alpha_2 \mathcal{K}_{2,h_{M-1}}^*) \cdots (\alpha_{h_2} \mathcal{K}_{h_2,h_1}^*) (\alpha_{h_1} \mathcal{K}_{h_1,h_0}^*) \beta_{h_0} \\ \vdots \\ \sum_{h_{M-1}=1}^N \cdots \sum_{h_1=1}^N \sum_{h_0=1}^N (\alpha_N \mathcal{K}_{N,h_{M-1}}^*) \cdots (\alpha_{h_2} \mathcal{K}_{h_2,h_1}^*) (\alpha_{h_1} \mathcal{K}_{h_1,h_0}^*) \beta_{h_0} \end{bmatrix}. \end{aligned} \quad (14)$$

Substitute Eq. (14) into Eq. (7), the solution to the interface problem at some query point \mathbf{x} can be estimated by

$$u(\mathbf{x}) \approx \int_{\Gamma} \Phi(\mathbf{x}, \mathbf{y}) \left(\sum_{i=0}^M w_i \sum_{h_i, \dots, h_1, h_0=1}^N (\alpha_{h_i} \mathcal{K}_{h_i, h_{i-1}}^*) \cdots (\alpha_{h_2} \mathcal{K}_{h_2, h_1}^*) (\alpha_{h_1} \mathcal{K}_{h_1, h_0}^*) \beta_{h_0} \mathbb{1}_{\partial\Omega_{h_i}} \right) dA_{\mathbf{y}}.$$

The weights are $w_i = 1 - \frac{1}{2}\delta_{i,M}$. Exchanging sums and integrals gives

$$u(\mathbf{x}) \approx \sum_{i=0}^M w_i \sum_{h_i, \dots, h_1, h_0=1}^N \int_{\partial\Omega_{h_i}} \Phi(\mathbf{x}, \mathbf{y}) \left((\alpha_{h_i} \mathcal{K}_{h_i, h_{i-1}}^*) \cdots (\alpha_{h_2} \mathcal{K}_{h_2, h_1}^*) (\alpha_{h_1} \mathcal{K}_{h_1, h_0}^*) \beta_{h_0} \right) dA_{\mathbf{y}}. \quad (15)$$

Note that $\left((\alpha_{h_i} \mathcal{K}_{h_i, h_{i-1}}^*) \cdots (\alpha_{h_2} \mathcal{K}_{h_2, h_1}^*) (\alpha_{h_1} \mathcal{K}_{h_1, h_0}^*) \beta_{h_0} \right)$ is a function of \mathbf{y} .

4 The Walk-on-Interfaces Method

In this section, we derive and present our *Walk-on-Interfaces* (WoI) estimator for the elliptic interface problem Eq. (2). We begin with a theorem serving as the backbone of our WoI estimators. Next, we propose a naive yet computationally intensive estimator. For better time performance, we exploit the linearity inherited in the naive estimator to develop a time-efficient alternative. Finally, we close this section by discussing the variance-reduced estimator and the gradient estimator.

4.1 A Theorem Towards Walk-on-Interfaces (WoI) Estimator

Observe that Eq. (15) writes $u(\mathbf{x})$ in a finite sum of boundary integrals. To establish our first WoI estimator for $u(\mathbf{x})$, it is sufficient to develop a Monte Carlo estimator for each inner product. We summarize an estimator for a boundary integral of the form

$$\int_{\partial\Omega_{h_i}} \Phi(\mathbf{x}, \mathbf{y}) (\mathcal{K}_{h_i, h_{i-1}}^* \cdots \mathcal{K}_{h_2, h_1}^* \mathcal{K}_{h_1, h_0}^* \beta_{h_0}) dA_{\mathbf{y}}$$

in Theorem 4.1.

We'll first introduce a notation for random variables before stating the theorem. Let $(h_0, h_1, \dots, h_i, \dots)$ be a sequence of interface or boundary indices. Let $Y_{(h_i, \dots, h_1, h_0)} \in \partial\Omega_{h_i}$ be a random variable in a Markov tree whose previous random state, $Y_{(h_{i-1}, \dots, h_1, h_0)}$, is located on $\partial\Omega_{h_{i-1}}$. Let $\mathbf{y}_{(h_i, \dots, h_1, h_0)} \in \partial\Omega_{h_i}$ be a realization of $Y_{(h_i, \dots, h_1, h_0)}$. As a shorthand notation, we denote $Y_{(h_i, \dots, h_1, h_0)}$ as Y_i , and $\mathbf{y}_{(h_i, \dots, h_1, h_0)}$ as \mathbf{y}_i , respectively. In the rest of this work, we will use the shorthand notation when the sequence of the interface indices can be inferred from equations or expressions.

With this notation, we introduce the following theorem.

Theorem 4.1. *Given a query point \mathbf{x} and a fixed set of $h_0, h_1, \dots, h_i \in \{1, \dots, N\}$. Let $\{Y_0, Y_1, \dots, Y_i, \dots\}$ be a Markov chain starting from \mathbf{x} such that $Y_i \in \partial\Omega_{h_i}$. Let $p_0(\mathbf{x}, \mathbf{y})$ and $p(\mathbf{x}, \mathbf{y})$ be any probability density functions (PDFs) denoting the transitional distribution of \mathbf{y} given \mathbf{x} . Define a family of functions*

$$Q_{(h_i, \dots, h_1, h_0)}^* = \begin{cases} \frac{\beta_{h_0}(Y_0)}{p_0(\mathbf{x}, Y_0)} & \text{if } i = 0 \\ Q_{(h_{i-1}, \dots, h_1, h_0)}^* \frac{K_{h_i, h_{i-1}}^*(Y_i, Y_{i-1})}{p(Y_{i-1}, Y_i)} & \text{if } i \geq 1 \end{cases}. \quad (16)$$

Then, $Q_{(h_i, \dots, h_1, h_0)}^* \Phi(\mathbf{x}, Y_i)$ is an unbiased estimator for

$$\int_{\partial\Omega_{h_i}} \Phi(\mathbf{x}, \mathbf{y}) (\mathcal{K}_{h_i, h_{i-1}}^* \cdots \mathcal{K}_{h_2, h_1}^* \mathcal{K}_{h_1, h_0}^* \beta_{h_0}) dA_{\mathbf{y}}.$$

i.e.

$$\int_{\partial\Omega_{h_i}} \Phi(\mathbf{x}, \mathbf{y}) (\mathcal{K}_{h_i, h_{i-1}}^* \cdots \mathcal{K}_{h_2, h_1}^* \mathcal{K}_{h_1, h_0}^* \beta_{h_0}) dA_{\mathbf{y}} = \mathbb{E} \left[Q_{(h_i, \dots, h_1, h_0)}^* \Phi(\mathbf{x}, Y_i) \right].$$

This theorem is proved in Appendix A.

4.2 Naive Walk-on-Interfaces

To translate Theorem 4.1 into practical algorithms, we begin by specifying key choices and essential components that contribute to our basic WoI estimators. We begin

by presenting our choice of transitional PDF in Section 4.2.1. Then, we state the resulting naive WoI estimator with the selected transitional PDF in Section 4.2.2. In Section 4.2.3, we explain our approach to sample the transitional PDF. Finally, we conclude our discussion of the naive WoI estimator by addressing the reuse of samples and Markov chains in Section 4.2.4.

4.2.1 Transitional Probability Function

The selection of appropriate probability density functions $p_0(\mathbf{x}, \mathbf{y}_0)$ and $p(\mathbf{y}_{i-1}, \mathbf{y}_i)$ is crucial for our algorithm. Ideal choices of transitional probability should achieve both efficiency, allowing easy sampling with fast algorithms, and accuracy, ensuring that the PDF closely approximates the integration kernel. While there can be many better choices, we use

$$p_0(\mathbf{x}, \mathbf{y}_0) = \frac{1}{|\partial\Omega_{h_0}|} \quad \text{and} \quad (17)$$

$$p(\mathbf{y}_{i-1}, \mathbf{y}_i) = \begin{cases} \frac{2}{m\alpha(m)} \frac{|(\mathbf{y}_i - \mathbf{y}_{i-1}) \cdot \mathbf{n}(\mathbf{y}_i)|}{q(\mathbf{y}_{i-1}, \mathbf{y}_i) |\mathbf{y}_i - \mathbf{y}_{i-1}|^m} & \text{if } h_{i-1} = h_i \\ \frac{1}{m\alpha(m)} \frac{|(\mathbf{y}_i - \mathbf{y}_{i-1}) \cdot \mathbf{n}(\mathbf{y}_i)|}{q(\mathbf{y}_{i-1}, \mathbf{y}_i) |\mathbf{y}_i - \mathbf{y}_{i-1}|^m} & \text{if } h_{i-1} \text{ is a descendant of } h_i. \\ \frac{1}{|\partial\Omega_{h_i}|} & \text{otherwise} \end{cases} \quad (18)$$

in all our implementations, where $q(\mathbf{y}_{i-1}, \mathbf{y}_i)$ is again the number of intersections between $\partial\Omega_i$ and a line (or a ray) passing through \mathbf{y}_{i-1} and \mathbf{y}_i . We will further explain this idea in Section 4.2.3.

4.2.2 The Naive WoI Estimator

Applying Theorem 4.1 to Eq. (15), we can write $u(\mathbf{x})$ by sums of expected values

$$u(\mathbf{x}) \approx \sum_{i=0}^M w_i \sum_{h_i, \dots, h_1, h_0=1}^N \left(\prod_{m=1}^i \alpha_{h_m} \right) \mathbb{E} [Q_{(h_i, \dots, h_1, h_0)}^* \Phi(x, Y_i)], \quad (19)$$

where $Q_{(h_i, \dots, h_1, h_0)}^*$ is defined in Eq. (16), with its corresponding $p_0(\mathbf{x}, \mathbf{y})$ and $p(\mathbf{x}, \mathbf{y})$ defined in Eq. (17) and Eq. (18), respectively.

Notice that we can write part of the transitional probability $p(\mathbf{y}_{i-1}, \mathbf{y}_i)$ as multiples

of $K_{h_i, h_{i-1}}^*(\mathbf{y}_{i-1}, \mathbf{y}_i) = \frac{1}{m\alpha(m)} \frac{(\mathbf{y}_{i-1} - \mathbf{y}_i) \cdot \mathbf{n}(\mathbf{y}_{i-1})}{|\mathbf{y}_{i-1} - \mathbf{y}_i|^m}$

$$p(\mathbf{y}_{i-1}, \mathbf{y}_i) = \begin{cases} \frac{2 \text{sign}[(\mathbf{y}_i - \mathbf{y}_{i-1}) \cdot \mathbf{n}(\mathbf{y}_i)]}{q(\mathbf{y}_{i-1}, \mathbf{y}_i)} K_{h_i, h_{i-1}}^*(\mathbf{y}_{i-1}, \mathbf{y}_i) & \text{if } h_{i-1} = h_i \\ \frac{\text{sign}[(\mathbf{y}_i - \mathbf{y}_{i-1}) \cdot \mathbf{n}(\mathbf{y}_i)]}{q(\mathbf{y}_{i-1}, \mathbf{y}_i)} K_{h_i, h_{i-1}}^*(\mathbf{y}_{i-1}, \mathbf{y}_i) & \text{if } h_{i-1} \text{ is a descendant of } h_i \\ \frac{1}{|\partial\Omega_{h_i}|} & \text{otherwise} \end{cases} \quad (20)$$

This observation allows us to decompose $Q_{(h_i, \dots, h_1, h_0)}^*$ into a product of a straightforward component,

$$Q_{(h_i, \dots, h_1, h_0)} = \begin{cases} \frac{\beta_{h_0}(Y_0)}{p_0(\mathbf{x}, Y_0)} & \text{if } i = 0 \\ \frac{1}{2} Q_{(h_{i-1}, \dots, h_1, h_0)} & \text{if } i \geq 1 \text{ and } h_{i-1} = h_i \\ Q_{(h_{i-1}, \dots, h_1, h_0)} & \text{if } i \geq 1 \text{ and } h_{i-1} \text{ is a descendant of } h_i \\ \frac{K_{h_i, h_{i-1}}^*(Y_i, Y_{i-1})}{p(Y_{i-1}, Y_i)} Q_{(h_{i-1}, \dots, h_1, h_0)} & \text{if } i \geq 1 \text{ and for any other } h_{i-1} \text{ and } h_i \end{cases} \quad (21)$$

and another more complicated component,

$$T_{(h_i, \dots, h_1, h_0)} = \begin{cases} 1 & \text{if } i = 0 \\ \prod_{m=1}^i q(Y_{m-1}, Y_m) \text{sign}[(Y_m - Y_{m-1}) \cdot \mathbf{n}(Y_m)] & \text{if } i \geq 1 \end{cases} \quad (22)$$

so that we don't need to evaluate $K_{h_i, h_{i-1}}^*(Y_i, Y_{i-1})$ in every update.

Hence, substituting the construction $Q_{(h_i, \dots, h_1, h_0)}^* = Q_{(h_i, \dots, h_1, h_0)} T_{(h_i, \dots, h_1, h_0)}$ gives

$$u(\mathbf{x}) \approx \sum_{i=0}^M w_i \sum_{h_i, \dots, h_1, h_0=1}^N \left(\prod_{m=1}^i \alpha_{h_m} \right) \mathbb{E} [Q_{(h_i, \dots, h_1, h_0)} T_{(h_i, \dots, h_1, h_0)} \Phi(x, Y_i)] \quad (23)$$

where $Q_{(h_i, \dots, h_1, h_0)}$ and $T_{(h_i, \dots, h_1, h_0)}$ are defined in Eq. (21) and Eq. (22), respectively. By linearity of expected value, the naive WoI estimator can be summarized in one single expected value,

$$u(\mathbf{x}) \approx \mathbb{E} \left[\sum_{i=0}^M w_i \sum_{h_i, \dots, h_1, h_0=1}^N \left(\prod_{m=1}^i \alpha_{h_m} \right) Q_{(h_i, \dots, h_1, h_0)} T_{(h_i, \dots, h_1, h_0)} \Phi(x, Y_i) \right] \quad (24)$$

4.2.3 Sampling Strategy

We now discuss our motivation for designing the transitional probabilities outlined in Eq. (17) and Eq. (18), and describe our method to sample \mathbf{y}_{i+1} given $\mathbf{y}_0, \mathbf{y}_1, \dots, \mathbf{y}_i$.

The transitional probability $p_0(\mathbf{x}, \mathbf{y}_0)$ is proposed to estimate the integral

$$\int_{\partial\Omega_{h_0}} \Phi(\mathbf{x}, \mathbf{y}) \beta_{h_0}(\mathbf{y}) dA_{\mathbf{y}},$$

whose kernel is $\Phi(\mathbf{x}, \mathbf{y})$. Since $\Phi(\mathbf{x}, \mathbf{y})$ is not proportional to any easy-to-sample distributions defined on $\partial\Omega_{h_0}$, we simply use a uniform distribution over $\partial\Omega_{h_0}$ for efficiency. Therefore, we sample a random point uniformly on $\partial\Omega_{h_0}$ to obtain \mathbf{y}_0 .

We define $p(\mathbf{x}, \mathbf{y})$ as the transitional probability to estimate integrals of the form

$$\int_{\partial\Omega_{h_i}} \Phi(\mathbf{x}, \mathbf{y}) (\mathcal{K}_{h_i, h_{i-1}}^* \cdots \mathcal{K}_{h_2, h_1}^* \mathcal{K}_{h_1, h_0}^* \beta_{h_0}) dA_{\mathbf{y}},$$

given $\mathbf{y}_0, \mathbf{y}_1, \dots, \mathbf{y}_{i-1}$, and when $i \geq 1$. Let $f = \mathcal{K}_{h_{i-1}, h_{i-2}}^* \mathcal{K}_{h_1, h_0}^* \beta_{h_0}$, then the target integral can be written as

$$\begin{aligned} \int_{\partial\Omega_{h_i}} \Phi(\mathbf{x}, \mathbf{y}) (\mathcal{K}_{h_i, h_{i-1}}^* f) dA_{\mathbf{y}} &= \int_{\partial\Omega_{h_i}} \Phi(\mathbf{x}, \mathbf{y}_i) \int_{\partial\Omega_{h_{i-1}}} K_{h_i, h_{i-1}}^*(\mathbf{y}_i, \mathbf{y}_{i-1}) f(\mathbf{y}_{i-1}) dA_{\mathbf{y}_{i-1}} dA_{\mathbf{y}_i} \\ &= \int_{\partial\Omega_{h_{i-1}}} f(\mathbf{y}_{i-1}) \int_{\partial\Omega_{h_i}} \Phi(\mathbf{x}, \mathbf{y}_i) K_{h_i, h_{i-1}}^*(\mathbf{y}_i, \mathbf{y}_{i-1}) dA_{\mathbf{y}_i} dA_{\mathbf{y}_{i-1}}. \end{aligned} \quad (25)$$

It suffices to estimate f from the given points $\mathbf{y}_0, \mathbf{y}_1, \dots, \mathbf{y}_{i-1}$, which leaves the inner integral,

$$\int_{\partial\Omega_{h_i}} \Phi(\mathbf{x}, \mathbf{y}_i) K_{h_i, h_{i-1}}^*(\mathbf{y}_i, \mathbf{y}_{i-1}) dA_{\mathbf{y}_i},$$

to be the only known part in Eq. (25).

We select the isotropic distribution, which is proportional to $K_{h_i, h_{i-1}}^*(\mathbf{y}_i, \mathbf{y}_{i-1})$. Also, h_{i-1} is a descendant of h_i (i.e. $\Omega_{h_{i-1}} \subseteq \Omega_{h_i}$), which promotes accuracy. In these cases, we obtain \mathbf{y}_i by first sampling a random direction \mathbf{d} , which defines a ray, $r(t) = t_{\geq 0} \mathbf{d} + \mathbf{y}_{i-1}$, originating at \mathbf{y}_{i-1} . Then we pick any intersection uniformly randomly between $r(t)$ and $\partial\Omega_i$ to be \mathbf{y}_i .

For a similar reason, we also use the isotropic distribution for the cases when $h_{i-1} = h_i$ (i.e. $\Omega_{h_{i-1}} = \Omega_{h_i}$). Notice that sampling a random ray this time does not guarantee the existence of an intersection between $r(t)$ and $\partial\Omega_i$. So, we must experience a time-wasting rejection sampling of ray direction before obtaining \mathbf{y}_i . As an alternative [32], we sample a line, $\ell(t) = t\mathbf{d} + \mathbf{y}_{i-1}$, in a random direction \mathbf{d} originating at \mathbf{y}_{i-1} , and set \mathbf{y}_i to be an arbitrary intersection between $r(t)$ and $\partial\Omega_{h_i}$.

However, for any other relation between h_{i-1} and h_i , it is not easy to sample $Y_i \in \partial\Omega_{h_i}$ under an isotropic distribution, since sampling a line or a ray following the same

procedure as previous does not always guarantee a hit on $\partial\Omega_i$. Rejection sampling is time-consuming, especially when Ω_{h_i} only occupies a tiny portion of the domain Ω . Therefore, even though the isotropic distribution represents $K_{h_i, h_{i-1}}^*(\mathbf{y}_i, \mathbf{y}_{i-1})$ precisely, we still use a uniform distribution over $\partial\Omega_{h_i}$ for the purpose of efficiency.

4.2.4 Reuse of Markov Chains

For each $i \in \{1, \dots, M\}$ and for each tuple of (h_0, h_1, \dots, h_i) , the naive WoI estimator Eq. (24) requires sampling the Markov chain, $\{Y_0, Y_1, \dots, Y_i\}$, to compute the expected value. While it is possible to initialize new Markov chains for each expected value, this approach is suboptimal in both memory storage and computational efficiency. The WoB estimator can achieve better time performance by reusing Markov chains generated for terms with $Q_{(h_i, \dots, h_1, h_0)}$ as part of the Markov chain for terms with $Q_{(h_j, \dots, h_i, \dots, h_1, h_0)}$, wherever $j > i$.

Let us fix a tuple $(h_0, h_1, \dots, h_i) \in \{1, 2, \dots, N\}^i$ and assume $\{\mathbf{y}_0, \mathbf{y}_1, \dots, \mathbf{y}_i\}$ to be a realization of the Markov chain for the term

$$\mathbb{E} \left[Q_{(h_i, \dots, h_1, h_0)} T_{(h_i, \dots, h_1, h_0)} \Phi(x, Y_i) \right].$$

Instead of sampling the Markov chain $\{Y_0, Y_1, \dots, Y_{i+1}\}$ with brand new samples, the next point $\mathbf{y}_{i+1} \in \partial\Omega_{h_{i+1}}$ can be sampled under the transitional probability $p(\mathbf{y}_i, \mathbf{y}_{i+1})$ so that $\{\mathbf{y}_0, \dots, \mathbf{y}_i, \mathbf{y}_{i+1}\}$ is a set of samples for the term

$$\mathbb{E} \left[Q_{(h_{i+1}, h_i, \dots, h_1, h_0)} T_{(h_{i+1}, h_i, \dots, h_1, h_0)} \Phi(x, Y_{i+1}) \right],$$

for any $h_{i+1} \in \{1, 2, \dots, N\}$.

Therefore, the points we need to sample for each observation of the expectation form a N -ary tree (with root \mathbf{x}) of height $M + 2$, where each branch of the tree is a Markov chain. We refer to such a tree as *Markov tree*. Figure 3 provides one toy example with $M = 1$, $N = 2$, for which

$$\begin{aligned} u(\mathbf{x}) \approx & \int_{\partial\Omega_1} \Phi(\mathbf{x}, \mathbf{y}) \beta_1(\mathbf{y}) dA_{\mathbf{y}} + \int_{\partial\Omega_2} \Phi(\mathbf{x}, \mathbf{y}) \beta_2(\mathbf{y}) dA_{\mathbf{y}} + \\ & \frac{1}{2} \int_{\partial\Omega_1} \Phi(\mathbf{x}, \mathbf{y}) (\alpha_1 \mathcal{K}_{1,1}^* \beta_1) dA_{\mathbf{y}} + \frac{1}{2} \int_{\partial\Omega_2} \Phi(\mathbf{x}, \mathbf{y}) (\alpha_2 \mathcal{K}_{2,1}^* \beta_1) dA_{\mathbf{y}} + \\ & \frac{1}{2} \int_{\partial\Omega_1} \Phi(\mathbf{x}, \mathbf{y}) (\alpha_1 \mathcal{K}_{1,2}^* \beta_2) dA_{\mathbf{y}} + \frac{1}{2} \int_{\partial\Omega_2} \Phi(\mathbf{x}, \mathbf{y}) (\alpha_2 \mathcal{K}_{2,2}^* \beta_2) dA_{\mathbf{y}}, \end{aligned}$$

as a special case of Eq. (15). The binary Markov tree of height three and an example of its realization over a nonconvex domain are visualized.

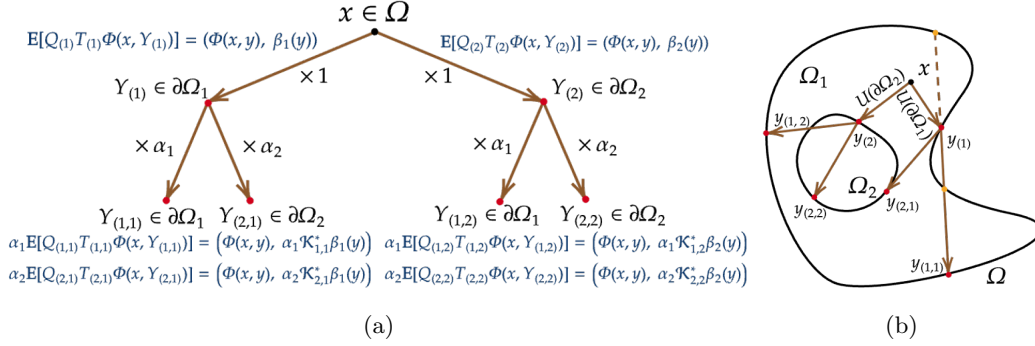


Figure 3: (a) The Markov tree, in which each branch is a Markov chain. We explicitly state which expected value approximates which boundary integral term in $u(\mathbf{x})$. Note that the boundary integrals are now written in the notation of L_2 inner products. The random variables are marked with full subscripts. (b) A realization of the Markov tree, where we reuse existing Markov chains. The red dots are selected to make statistical contribution to the expected value. The dashed line is the line $\ell(t)$ we sampled, and the yellow dots are the unselected intersections. $\mathbf{y}_{(1)}$ and $\mathbf{y}_{(2)}$ are uniformly sampled on $\partial\Omega_1$ and $\partial\Omega_2$, respectively, since $p_0(\mathbf{x}, \mathbf{y}_{h_0})$ is uniform. Given $\mathbf{y}_{(1)}$, $\mathbf{y}_{(1,1)}$ is sampled under isotropic distribution, since $h_1 = h_0 = 1$, while $\mathbf{y}_{(2,1)}$ is sampled uniformly on $\partial\Omega_2$, as $h_0 = 1$ is not a descendant of $h_1 = 2$. Given $\mathbf{y}_{(2)}$, $\mathbf{y}_{(1,2)}$ and $\mathbf{y}_{(2,2)}$ are sampled on $\partial\Omega_1$ and $\partial\Omega_2$, respectively, under isotropic distribution.

4.3 Acceleration

Generating samples for the naive WoI requires traversing the N -ary Markov tree, which yields exponential time complexity. In each traversal, the number of random variables we need to sample is $\sum_{i=1}^M N^i$. If we sample \mathcal{T} Markov trees for the expected value in Eq. (24), the naive WoI estimator relies on $\mathcal{T} \sum_{i=0}^M N^i$ points on interfaces to complete the estimation. This quantity grows rapidly with increasing N and escalates exponentially with respect to M . Therefore, it is desirable to avoid the tree traversal to maintain a reasonable estimation time while keeping the quality of the estimator.

4.3.1 The WoI Estimator

We avoid tree traversal by leveraging the coefficient, α_{h_i} , in the naive WoI estimator, which is formalized in Theorem 4.2 and proven in Appendix B.

Theorem 4.2. *Let H_0, H_1, \dots, H_i be independent discrete random variables with PDF*

$$\mathbb{P}(H_i = n) = \begin{cases} \frac{1}{N} & \forall n \in \{1, \dots, N\}, \text{ when } i = 0 \\ \frac{|\alpha_n|}{\|\alpha\|_1} & \forall n \in \{1, \dots, N\}, \text{ when } i \geq 1 \end{cases}, \quad (26)$$

where $\|\cdot\|_1$ is the ℓ_1 norm. It can be shown that

$$\begin{aligned} & \sum_{h_i, \dots, h_1, h_0=1}^N \int_{\partial\Omega_{h_i}} \Phi(\mathbf{x}, \mathbf{y}) \left((\alpha_{h_i} \mathcal{K}_{h_i, h_{i-1}}^*) \cdots (\alpha_{h_2} \mathcal{K}_{h_2, h_1}^*) (\alpha_{h_1} \mathcal{K}_{h_1, h_0}^*) \beta_{h_0} \right) dA_{\mathbf{y}} \\ &= N \|\boldsymbol{\alpha}\|_1^i \mathbb{E}_{H_i, \dots, H_0} \left[\prod_{m=1}^i \text{sign}(\alpha_{H_m}) \int_{\partial\Omega_{H_i}} \Phi(\mathbf{x}, \mathbf{y}) \left(\mathcal{K}_{H_i, H_{i-1}}^* \cdots \mathcal{K}_{H_1, H_0}^* \beta_{H_0} dA_{\mathbf{y}} \right) \right]. \end{aligned}$$

Applying the result in Theorem 4.2 to Eq. (15), we have

$$u(\mathbf{x}) \approx \sum_{i=0}^M w_i N \|\boldsymbol{\alpha}\|_1^i \mathbb{E}_{H_i, \dots, H_0} \left[\prod_{m=1}^i \text{sign}(\alpha_{H_m}) \int_{\partial\Omega_{H_i}} \Phi(\mathbf{x}, \mathbf{y}) \left(\mathcal{K}_{H_i, H_{i-1}}^* \cdots \mathcal{K}_{H_1, H_0}^* \beta_{H_0} dA_{\mathbf{y}} \right) \right].$$

Then by Theorem 4.1 again, the WoI estimator is

$$u(\mathbf{x}) \approx \sum_{i=0}^M w_i N \|\boldsymbol{\alpha}\|_1^i \mathbb{E}_{H_i, \dots, H_0} \left[\prod_{m=1}^i \text{sign}(\alpha_{H_m}) \mathbb{E}_{Y_i} \left[Q_{(H_i, \dots, H_1, H_0)} T_{(H_i, \dots, H_1, H_0)} \Phi(\mathbf{x}, Y_i) \right] \right], \quad (27)$$

for which we substituted $Q_{(H_i, \dots, H_1, H_0)} T_{(H_i, \dots, H_1, H_0)}$ for $Q_{(H_i, \dots, H_1, H_0)}^*$.

4.3.2 A Summary of the WoI Procedure

Based on our design of the WoI estimator, we outline the process for estimating $u(\mathbf{x})$ as presented in Eq. (27). After fixing M , we first sample \mathcal{S} sets of discrete random variables H_0, H_1, \dots, H_M under the distribution defined in Eq. (26) for the outer expected value, $\mathbb{E}_{H_M, \dots, H_1, H_0}$. By doing so, we *schedule* the interface or the boundary where the random variables Y_0, Y_1, \dots, Y_M are located. Then, for each set of scheduled locations, $\{h_0, h_1, \dots, h_M\}$, we sample \mathcal{W} *walkers* that walk $M+1$ steps each. The *trajectory* of each walker is a Markov chain $\{Y_0, Y_1, \dots, Y_M\}$ such that $Y_i \in \partial\Omega_{h_i}$. The transitional probabilities for the Markov chain $\{Y_0, Y_1, \dots, Y_M\}$ with is defined in Eq. (17) and Eq. (18), and the sampling strategy for Y_i 's is detailed in Section 4.2.3.

Hence, we compute the inner expected value, $\mathbb{E}_{Y_i}[\cdot]$, to complete the estimation of $u(\mathbf{x})$. We present the pseudocode of the WoI estimator in Algorithm 1 that computes the expected value, and Algorithm 2 that samples the states, Y_i 's.

In Figure 4, we show all possible schedules of the WoI estimator, each with one example trajectory, when $N = 2$ and $M = 1$.

Algorithm 1 Wrapper Function for WoI Estimator

Input: Query point \mathbf{x} , number of interfaces N , problem dimension d ,
 integration kernel $K_{i,j}^*(\mathbf{x}, \mathbf{y}) = \frac{1}{d\alpha(d)} \frac{(\mathbf{x}-\mathbf{y}) \cdot \mathbf{n}(\mathbf{x})}{|\mathbf{x}-\mathbf{y}|^m}$, where m is the dimension,
 constant array $\boldsymbol{\alpha} = [\alpha_1 \ \alpha_2 \ \dots \ \alpha_N]$,
 boundary and interface conditions $\boldsymbol{\beta} = [\beta_1 \ \beta_2 \ \dots \ \beta_N]$,
 fundamental solution $\Phi(\mathbf{x}, \mathbf{y})$,
 \mathcal{S} sets of interface schedules, \mathcal{W} walkers, $M + 1$ steps for each walker.

Output: Estimated solution $u(\mathbf{x})$.

```

1: function WOIESTIMATOR( $\mathbf{x}, K_{i,j}^*(\mathbf{x}, \mathbf{y}), \boldsymbol{\beta}, \Phi(\mathbf{x}, \mathbf{y}), \boldsymbol{\alpha}, \mathcal{S}, M, \mathcal{C}$ )
2:    $u(\mathbf{x}) = 0$ 
3:   for  $s = 1$  to  $\mathcal{S}$  do
4:      $S \leftarrow [h_0, h_1, \dots, h_M]$   $\triangleright$  sample  $H_0, H_1, \dots, H_M$  to obtain the  $s^{\text{th}}$  interface schedule
5:      $u_s = 0$ 
6:     for  $w = 1$  to  $\mathcal{W}$  do  $\triangleright$  walkers start walking
7:        $u_w = \text{WoI}(\mathbf{x}, K_{i,j}^*(\mathbf{x}, \mathbf{y}), \Phi(\mathbf{x}, \mathbf{y}), \boldsymbol{\alpha}, \boldsymbol{\beta}, M, S)$   $\triangleright$  Algorithm 2
8:        $u_s = u_s + (u_w - u_s)/w$   $\triangleright$  Welfords algorithm for  $\mathbb{E}_{Y_i}$ 
9:      $u(\mathbf{x}) = u(\mathbf{x}) + (u_s - u(\mathbf{x}))/s$   $\triangleright$  Welfords algorithm for expectation for  $\mathbb{E}_{H_i, \dots, H_0}$ 
10:  return  $N * u(\mathbf{x})$ 
  
```

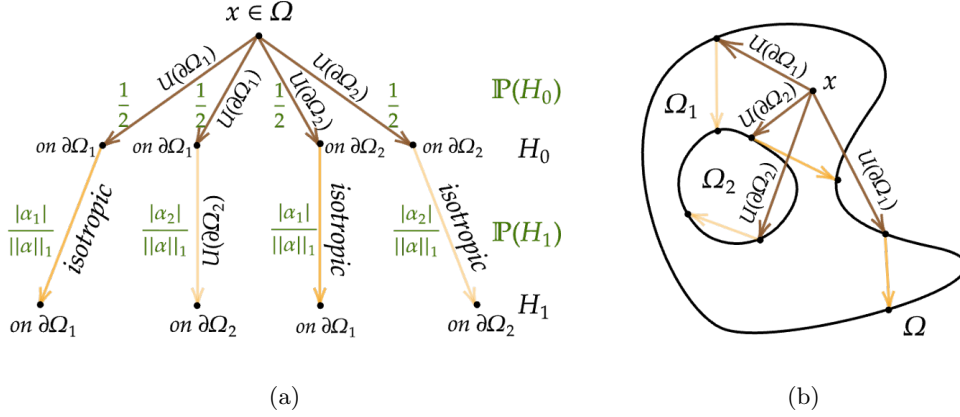


Figure 4: Consider an domain with one interface ($N = 2$) and each walker walks two steps ($M = 1$). Assume $|\alpha_1| > |\alpha_2|$. Then, $\partial\Omega_1$ is more likely to be scheduled than $\partial\Omega_2$ starting from H_1 . By construction, we have $\mathbb{P}(H_0 = n) = \frac{1}{2}$, and $\mathbb{P}(H_1 = n) = \frac{|\alpha_n|}{\|\boldsymbol{\alpha}\|_1}$, $\forall n \in \{1, 2\}$. (a) A diagram for all possible WoI schedules. The black dots indicate Y_i 's. For points at the same height, a darker-colored arrow pointing toward them indicates a higher likelihood of the interface being scheduled. (b) One example trajectory for each possible WoI schedule.

Algorithm 2 The WoI Estimator

```

1: function WoI( $\mathbf{x}, K_{i,j}^*(\mathbf{x}, \mathbf{y}), \Phi(\mathbf{x}, \mathbf{y}), \alpha, \beta, M, S$ )
2:    $u_w \leftarrow 0, T \leftarrow 1, \text{weight} \leftarrow 1.$ 
3:   for  $i = 0$  to  $M$  do
4:     if  $i == M$  then
5:        $\text{weight} \leftarrow 0.5$   $\triangleright$  truncation
6:        $h_i \leftarrow S(i)$ 
7:       if  $i == 0$  then  $\triangleright$  transitional PDF is  $p_0(\mathbf{x}, \mathbf{y})$ 
8:          $\mathbf{y}_i \leftarrow \text{Unif}(\partial\Omega_{h_i})$ 
9:          $Q = \beta_{h_i}(\mathbf{y}_i) / \frac{1}{|\partial\Omega_{h_i}|}$ 
10:         $u_w = u_w + \text{weight} * \|\alpha\|_1^i * Q * T * \Phi(\mathbf{x}, \mathbf{y}_i)$ 
11:      else  $\triangleright$  transitional PDF is  $p(\mathbf{x}, \mathbf{y})$ 
12:         $h_{i-1} \leftarrow S(i-1)$   $\triangleright i \geq 1$ 
13:        if  $h_{i-1} = h_i$  then
14:           $\mathbf{d} \leftarrow$  an isotropic direction
15:           $q(\mathbf{y}_{i-1}, \mathbf{y}_i) \leftarrow$  # of intersections between  $\partial\Omega_{h_i}$  and a line  $\ell(t) = t\mathbf{d} + \mathbf{y}_{i-1}$ 
16:           $\mathbf{y}_i \leftarrow$  any of the  $q(\mathbf{y}_{i-1}, \mathbf{y}_i)$  intersections
17:           $Q \leftarrow Q * 0.5$ 
18:        else if  $h_{i-1}$  a descendant of  $h_i$  then
19:           $\mathbf{d} \leftarrow$  an isotropic direction
20:           $q(\mathbf{y}_{i-1}, \mathbf{y}_i) \leftarrow$  # of intersections between  $\partial\Omega_{h_i}$  and a ray  $r(t) = t_{\geq 0}\mathbf{d} + \mathbf{y}_{i-1}$ 
21:           $\mathbf{y}_i \leftarrow$  any of the  $q(\mathbf{y}_{i-1}, \mathbf{y}_i)$  intersections
22:           $Q \leftarrow Q * 1$ 
23:        else
24:           $q(\mathbf{y}_{i-1}, \mathbf{y}_i) \leftarrow 1$ 
25:           $\mathbf{y}_i \leftarrow \text{Unif}(\partial\Omega_{h_i})$ 
26:           $Q = Q * K_{h_i, h_{i-1}}^*(\mathbf{y}_i, \mathbf{y}_{i-1}) / \frac{1}{|\partial\Omega_{h_i}|}$ 
27:           $T = T * q(\mathbf{y}_{i-1}, \mathbf{y}_i) * \text{sign}[(\mathbf{y}_i - \mathbf{y}_{i-1}) \cdot \mathbf{n}(\mathbf{y}_i)]$ 
28:           $u_w = u_w + \text{weight} * \|\alpha\|_1^i * [\prod_{m=0}^i \text{sign}(\alpha_{h_m})] * Q * T * \Phi(\mathbf{x}, \mathbf{y}_i)$ 
29:    return  $u_w$ 

```

4.4 Variance Reduction

As for the WoB, we want the WoI to be an effective estimator with small variance. We follow a similar strategy [32] to enhance the performance of WoI. Meanwhile, we must point out that there are many other importance sampling methods that can improve the quality of the WoI estimator.

For some fixed M , the variance-reduced WoI estimator depends on two simultaneous walkers for each query point. We divide the first interface (or boundary), $\partial\Omega_{H_0}$, into two parts, $\partial\Omega_{H_0}^+$ and $\partial\Omega_{H_0}^-$ such that

$$\partial\Omega_{H_0}^+ = \{\mathbf{y} \in \partial\Omega : \beta_{H_0}(\mathbf{y}) \geq 0\}, \quad \partial\Omega_{H_0}^- = \{\mathbf{y} \in \partial\Omega : \beta_{H_0}(\mathbf{y}) < 0\}.$$

Instead of sampling Y_0 uniformly over $\partial\Omega_{H_0}$ in the first step of WoI, we introduce two random variables, $Y_0^{(1)}$ and $Y_0^{(2)}$, under a uniform distribution over $\partial\Omega_{H_0}^+$ and $\partial\Omega_{H_0}^-$, respectively. First, we sample two points $\mathbf{y}_0^{(1)} \in \partial\Omega_{H_0}^+$ and $\mathbf{y}_0^{(2)} \in \partial\Omega_{H_0}^-$ as realizations of $Y_0^{(1)}$ and $Y_0^{(2)}$, respectively. Then, starting from $\mathbf{y}_0^{(1)}$ and $\mathbf{y}_0^{(2)}$ respectively, we construct two Markov chains, namely $\{Y_0^{(1)}, Y_1^{(1)}, \dots, Y_M^{(1)}\}$ and $\{Y_0^{(2)}, Y_1^{(2)}, \dots, Y_M^{(2)}\}$ such that $Y_i^{(k)} \in \partial\Omega_{H_i}$, $\forall k \in \{1, 2\}$. We repeat the standard WoI sampling strategy as described in Section 4.2.3 for both Markov chains. Finally, we sum up the estimation from both Markov chains.

In summary, the variance-reduced WoI estimator is

$$u(\mathbf{x}) \approx \sum_{i=0}^M w_i N \|\boldsymbol{\alpha}\|_1^i \mathbb{E}_{H_i, \dots, H_0} \left[\prod_{m=1}^i \text{sign}(\alpha_{H_m}) \mathbb{E}_{Y_i} \left[\sum_{k=1}^2 Q_{(H_i, \dots, H_1, H_0)}^{(k)} T_{(H_i, \dots, H_1, H_0)}^{(k)} \Phi(\mathbf{x}, Y_i^{(k)}) \right] \right], \quad (28)$$

in which $p_0^{(1)}(\mathbf{x}, \mathbf{y}) = \frac{1}{|\partial\Omega_{H_0}^+|}$, $p_0^{(2)}(\mathbf{x}, \mathbf{y}) = \frac{1}{|\partial\Omega_{H_0}^-|}$, $p(\mathbf{x}, \mathbf{y})$ is defined in Eq. (18),

$$Q_{(h_i, \dots, h_1, h_0)}^{(k)} = \begin{cases} \frac{\beta_{h_0}(Y_0^{(k)})}{p_0^{(k)}(\mathbf{x}, Y_0^{(k)})} & \text{if } i = 0 \\ \frac{1}{2} Q_{(h_{i-1}, \dots, h_1, h_0)}^{(k)} & \text{if } i \geq 1 \text{ and } h_{i-1} = h_i \\ Q_{(h_{i-1}, \dots, h_1, h_0)}^{(k)} & \text{if } i \geq 1 \text{ and } h_{i-1} \text{ is a descendant of } h_i \\ \frac{K_{h_i, h_{i-1}}^*(Y_i^{(k)}, Y_{i-1}^{(k)})}{p(Y_{i-1}^{(k)}, Y_i^{(k)})} Q_{(h_{i-1}, \dots, h_1, h_0)}^{(k)} & \text{if } i \geq 1 \text{ and for any other } h_{i-1} \text{ and } h_i \end{cases}, \quad (29)$$

and

$$T_{(h_i, \dots, h_1, h_0)}^{(k)} = \begin{cases} 1 & \text{if } i = 0 \\ \prod_{m=1}^i q(Y_{m-1}^{(k)}, Y_m^{(k)}) \text{sign}[(Y_m^{(k)} - Y_{m-1}^{(k)}) \cdot \mathbf{n}(Y_m^{(k)})] & \text{if } i \geq 1 \end{cases}. \quad (30)$$

Algorithm 3 provides a detailed explanation of the variance-reduced WoI method, which can replace line 7 of Algorithm 1 whenever necessary. Figure 5 demonstrates all possible schedules that can occur in a variance-reduced WoI estimator. For each type of schedule, a sampled trajectory is also provided within the same figure.

4.5 Gradient Estimation

The WoI estimator inherits the property from the WoB that we obtain a gradient estimation with almost no additional cost. This feature enables a fully Monte Carlo approach for computing the gradient of the solution to the elliptic interface problem. In contrast, prior method [12] relied on applying finite-differences to Monte Carlo estimates of $u(\mathbf{x})$.

Algorithm 3 The Variance Reduced WoI Estimator

```

1: function VARREDUCEDWOI( $\mathbf{x}$ ,  $K_{i,j}^*(\mathbf{x}, \mathbf{y})$ ,  $\Phi(\mathbf{x}, \mathbf{y})$ ,  $\alpha$ ,  $\beta$ ,  $M$ ,  $S$ )
2:    $u_w \leftarrow 0$ ,  $T^{(1)} \leftarrow 1$ ,  $T^{(2)} \leftarrow 1$ , weight  $\leftarrow 1$ .
3:   for  $i = 0$  to  $M$  do
4:     if  $i == M$  then
5:       weight  $\leftarrow 0.5$   $\triangleright$  truncation
6:        $h_i \leftarrow S(i)$ 
7:       if  $i == 0$  then  $\triangleright$  transitional PDF is  $p_0(\mathbf{x}, \mathbf{y})$ 
8:          $\mathbf{y}_i^{(1)} \leftarrow \text{Unif}(\partial\Omega_{h_i}^+)$ ,  $\mathbf{y}_i^{(2)} \leftarrow \text{Unif}(\partial\Omega_{h_i}^-)$ 
9:          $Q^{(1)} = \beta_{h_i}(\mathbf{y}_i^{(1)}) / \frac{1}{|\partial\Omega_{h_i}^+|}$ ,  $Q^{(2)} = \beta_{h_i}(\mathbf{y}_i^{(2)}) / \frac{1}{|\partial\Omega_{h_i}^-|}$ 
10:         $u_w = u_w + \text{weight} * \|\alpha\|_1^i * (\sum_{k=1}^2 Q^{(k)} * T^{(k)} * \Phi(\mathbf{x}, \mathbf{y}_i^{(k)}))$ 
11:      else  $\triangleright$  transitional PDF is  $p(\mathbf{x}, \mathbf{y})$ 
12:         $h_{i-1} \leftarrow S(i-1)$   $\triangleright i \geq 1$ 
13:        for  $k = 1$  to  $2$  do
14:          if  $h_{i-1} = h_i$  then
15:             $\mathbf{d} \leftarrow$  an isotropic direction
16:             $q(\mathbf{y}_{i-1}^{(k)}, \mathbf{y}_i^{(k)}) \leftarrow$  # of intersections between  $\partial\Omega_{h_i}$  and line  $\ell(t) = t\mathbf{d} + \mathbf{y}_{i-1}^{(k)}$ 
17:             $\mathbf{y}_i^{(k)} \leftarrow$  any of the  $q(\mathbf{y}_{i-1}^{(k)}, \mathbf{y}_i^{(k)})$  intersections
18:             $Q^{(k)} \leftarrow Q^{(k)} * 0.5$ 
19:          else if  $h_{i-1}$  a descendant of  $h_i$  then
20:             $\mathbf{d} \leftarrow$  an isotropic direction
21:             $q(\mathbf{y}_{i-1}^{(k)}, \mathbf{y}_i^{(k)}) \leftarrow$  # of intersections between  $\partial\Omega_{h_i}$  and ray  $r(t) = t_{\geq 0}\mathbf{d} + \mathbf{y}_{i-1}^{(k)}$ 
22:             $\mathbf{y}_i^{(k)} \leftarrow$  any of the  $q(\mathbf{y}_{i-1}^{(k)}, \mathbf{y}_i^{(k)})$  intersections
23:             $Q^{(k)} \leftarrow Q^{(k)} * 1$ 
24:          else
25:             $q(\mathbf{y}_{i-1}^{(k)}, \mathbf{y}_i^{(k)}) \leftarrow 1$ 
26:             $\mathbf{y}_i^{(k)} \leftarrow \text{Unif}(\partial\Omega_{h_i})$ 
27:             $Q^{(k)} = Q^{(k)} * K_{h_i, h_{i-1}}^*(\mathbf{y}_i^{(k)}, \mathbf{y}_{i-1}^{(k)}) / \frac{1}{|\partial\Omega_{h_i}|}$ 
28:             $T^{(k)} = T^{(k)} * q(\mathbf{y}_{i-1}^{(k)}, \mathbf{y}_i^{(k)}) * \text{sign}[(\mathbf{y}_i^{(k)} - \mathbf{y}_{i-1}^{(k)}) \cdot \mathbf{n}(\mathbf{y}_i^{(k)})]$ 
29:           $u_w = u_w + \text{weight} * \|\alpha\|_1^i * [\prod_{m=0}^i \text{sign}(\alpha_{h_m})] * (\sum_{k=1}^2 Q^{(k)} * T^{(k)} * \Phi(\mathbf{x}, \mathbf{y}_i^{(k)}))$ 
30:  return  $u_w$ 

```

The estimator for $\nabla u(\mathbf{x})$ is obtained by simply taking the gradient of $\Phi(\mathbf{x}, \mathbf{y})$ in the estimator of $u(\mathbf{x})$. Hence, the WoI gradient estimator is

$$\nabla u(\mathbf{x}) \approx \mathbb{E} \left[\sum_{i=0}^M w_i \sum_{h_i, \dots, h_1, h_0=1}^N \left(\prod_{m=1}^i \alpha_{h_m} \right) Q_{(h_i, \dots, h_1, h_0)} T_{(h_i, \dots, h_1, h_0)} \nabla_{\mathbf{x}} \Phi(\mathbf{x}, Y_i) \right], \quad (31)$$

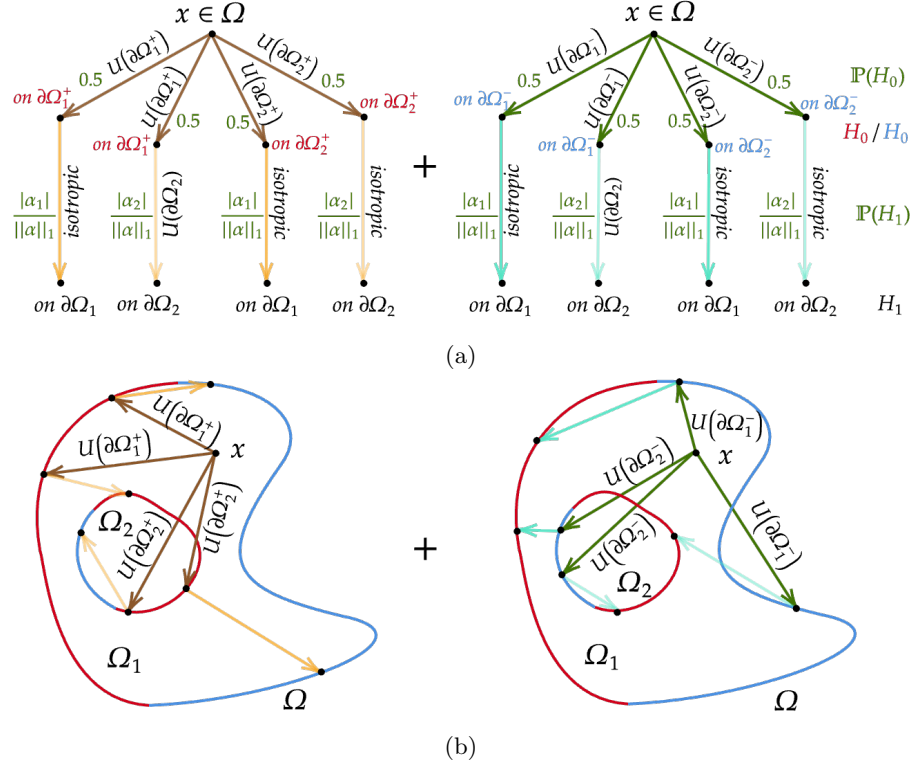


Figure 5: Consider the domain under the same setup as the one in Figure 4. We still let $|\alpha_1| > |\alpha_2|$, such that $\mathbb{P}(H_0 = n) = \frac{1}{2}$, and $\mathbb{P}(H_1 = n) = \frac{|\alpha_n|}{\|\alpha\|_1}$, $\forall n \in \{1, 2\}$. (a) A diagram for all possible variance-reduced WoI schedules. The black dots indicate $Y_i^{(k)}$, where $k \in \{1, 2\}$. For points at the same height, a darker-colored arrow pointing toward them indicates a higher likelihood of the interface being scheduled. (b) One example trajectory for each possible variance-reduced WoI schedules.

while a variance-reduced WoI gradient estimator is

$$\nabla u(\mathbf{x}) \approx \sum_{i=0}^M w_i N \|\alpha\|_1^i \mathbb{E}_{H_i, \dots, H_0} \left[\prod_{m=1}^i \text{sign}(\alpha_{H_m}) \mathbb{E}_{Y_i} \left[\sum_{k=1}^2 Q_{(H_i, \dots, H_1, H_0)}^{(k)} T_{(H_i, \dots, H_1, H_0)}^{(k)} \nabla_{\mathbf{x}} \Phi(\mathbf{x}, Y_i^{(k)}) \right] \right]. \quad (32)$$

The WoI gradient estimator allows us to use all walkers and trajectories we generated for the WoI estimator to estimate $\nabla u(\mathbf{x})$, which gives almost no extra cost.

4.6 Implementation Considerations

We outline some key implementation details of our WoI estimator in this section. The discussion includes proper representation of computational domains, parallelization

of walkers, batch estimation of query points, and the management of floating-point precision.

Domain Definitions. There are many common ways to represent geometries, such as signed distance functions (SDFs), level sets, surface meshes, and implicit functions. Each representation offers trade-offs in terms of accuracy, computational cost, and ease of sampling under certain distributions. According to our design of WoI and variance-reduced WoI estimators, we prioritize representations that facilitate uniform sampling over the domain boundary and efficient computation of ray-mesh and line-mesh intersections. To this end, we adopt surface meshes equipped with axis-aligned bounding box (AABB) tree structures, which are well-suited for both uniform boundary sampling and geometric intersection queries. We additionally accept implicit function representations in cases where established algorithms are available for uniform sampling on the boundary and for performing intersection tests.

Parallelization of Walkers. It is well known that Monte Carlo methods are, in general, highly parallelizable. This principle extends naturally to the WoI estimator. Suppose each of the \mathcal{W} walkers performs M steps, and assume that we sampled H_1, H_2, \dots, H_M with realizations h_1, h_2, \dots, h_M as one schedule of interfaces. When the i^{th} states of several walkers are located on the same boundary, they can be generated in parallel, provided that the hierarchical relationship between h_{i-1} and h_i falls in one of the three cases of $p(\mathbf{y}_{i-1}, \mathbf{y}_i)$.

Batch Estimation with Shared Trajectories. The WoI estimator, its gradient estimator, and their variance-reduced counterparts all require constructing trajectories for walkers by sampling the interfaces (or the boundary). However, building these stochastic trajectories is computationally expensive. While it is possible to generate independent trajectories for each query point, we instead reuse the same set of trajectories across multiple query points. To simplify the implementation, we randomly shuffle the query points and assign the same set of trajectories to those points with nearby indices in the shuffled list. Hence, we obtain a vectorized evaluation of the WoI estimator, allowing us to compute the solution to the interface problem at a batch of query points simultaneously.

Although this approach introduces correlations in the estimation errors at different spatial locations, it significantly reduces the overall computational cost. With an appropriate choice of batch size, the estimator retains sufficient stochastic properties, and the resulting high-frequency error can still be well-captured. We recommend that the batch size is no larger than 0.5% of the total number of query points.

Floating-point Precision. All the estimators developed so far require the evaluation of either $\Phi(\mathbf{x}, Y_i)$ or $\nabla\Phi(\mathbf{x}, Y_i)$. To avoid repeatedly evaluating the Green’s function

and its gradient, it is desirable to allow vectorized input for both functions. Achieving this level of parallelism requires storing a large number of (\mathbf{x}, Y_i) pairs in memory. To improve storage efficiency and maximize batch size, we store the query point vector, \mathbf{x} , and the state of the walkers, Y_i , in single-precision floating-point format whenever possible. This reduction in memory footprint allows for larger-scale vectorized operations while maintaining sufficient numerical accuracy for estimation.

5 Results

In this section, we first evaluate the accuracy and convergence behaviour of the WoI estimator and its variance-reduced counterpart. We provide examples to show how our Monte Carlo estimators solve problems with different domain geometries and how they naturally extend to higher-dimensional domains. Next, we integrate a neural network into our method to obtain a continuous representation of the solution and to smooth out the high-frequency errors of the Monte Carlo estimator. This approach leverages the neural network’s inductive bias toward smooth functions, providing both improved accuracy and a convenient functional form for downstream evaluation. Finally, we conclude this section by demonstrating the practical effectiveness of the WoI framework in solving interface problems under different application scenarios.

Correctness. We begin by evaluating the accuracy of the WoI estimator. Let $\hat{u}(\mathbf{x})$ denote the estimated solution and $u(\mathbf{x})$ represent the ground truth. Given that the solution to the interface problem in Eq. (2) is unique up to a constant, we anticipate that the WoI estimation deviates from the ground truth by a constant offset. To more effectively quantify the estimation error, $e(\mathbf{x})$, we align the estimated solution by shifting it to match the ground truth at a fixed reference point, \mathbf{x}_{ref} ,

$$e(\mathbf{x}) = |u(\mathbf{x}) - [\hat{u}(\mathbf{x}) - \hat{u}(\mathbf{x}_{ref}) + u(\mathbf{x}_{ref})]|.$$

In our examples, we will consider the L_2 norm of the error, $\|e(\mathbf{x})\|_2$ and the relative L_2 norm of the error, $\frac{\|e(\mathbf{x})\|_2}{\|u(\mathbf{x})\|_2}$.

Example 1. A smooth harmonic function in 2D. As the first example, we examine the performance of the WoI estimator and the variance-reduced WoI estimator over a two-dimensional domain, for which the ground truth is a C^∞ function. Since any harmonic function satisfies the elliptic interface problem, we let the first ground truth be $u(x_1, x_2) = x_1^3 - 3x_1x_2^2$. To break the symmetry of the solution, we shift the domain away from the origin and solve the interface problem on a circle of radius 2 centered at $(0.5, -0.5)$.

Table 1: Parameters for the Nested Ellipsoids in Example 2.

Ellipsoid Name	center (\mathbf{c})	\mathbf{A}	σ
Ω_1	$(1.3, 0, \dots, 0)$	$\text{diag}(\mathbf{A}) = [1, 0.9, 1.2, \dots, 1.2]$	1.1
Ω_2	$(1.4, 0, \dots, 0)$	$\text{diag}(\mathbf{A}) = [1.5, 3.2, 2, \dots, 2]$ with $A(1, 2) = A(2, 1) = -1$	1.3
Ω_3	$(1.6, 0, \dots, 0)$	$\text{diag}(\mathbf{A}) = [8, 6, 4, \dots, 4]$ with $A(1, 2) = A(2, 1) = -2$	0.9

We allow both estimators to walk $M = 4$ steps. Furthermore, we compute the expectations with respect to $\mathbb{E}_{Y_i}[\cdot]$ using the same total number of samples. In the variance-reduced WoI estimator, each sample of $\mathbb{E}_{Y_i}[\cdot]$ involves contributions from both $Y_i^{(1)}$ and $Y_i^{(2)}$. Therefore, we generate the same number of samples for each of $Y_i^{(k)}$, where $k \in \{1, 2\}$, as the number of Y_i samples used in the standard WoI estimator. Since the variance-reduced estimator relies on two independent walkers per sample, it inherently requires twice as many walkers as the standard WoI estimator. To ensure a fair comparison in terms of computational cost and estimation quality, we match the total number of walkers used in both methods. When $\mathcal{W} = 10^7$, we observe that the variance-reduced WoI estimator outperforms the WoI estimator. The corresponding results for both methods are shown in Figure 6, which visualizes the estimated solutions and the pointwise errors relative to the ground truth.

Example 2. Potential of a point charge at the origin. In the second example, we test our estimators with higher-dimensional ellipsoidal domains. The ellipsoids are defined via implicit surfaces of the form $(\mathbf{x} - \mathbf{c})^T \mathbf{A}(\mathbf{x} - \mathbf{c}) = 1$, where \mathbf{c} is the center, and \mathbf{A} is a positive definite matrix. The ground truth function, $u : \mathbb{R}^n \rightarrow \mathbb{R}$, is defined as $u(\mathbf{x}) = \|\mathbf{x}\|^{2-n}$, where $n \geq 3$. This function arises naturally in physics: in electrostatics, it represents the potential field generated by a unit point charge at the origin in \mathbb{R}^n ; in gravitational theory, it corresponds to the gravitational potential of a point mass.

Due to the singularity of $u(\mathbf{x})$ at the origin, we shift the domain to exclude the origin so that the singularity is not approximated. The domains consist of three nested ellipsoids. We name the outer-most ellipsoid Ω_1 , the middle ellipsoid Ω_2 , and the inner-most ellipsoid Ω_3 . The detailed parameters of the domain are recorded in Table 1.

We visualize the 3D domain and its associated estimated solution on the equatorial plane in Figure 7. For domains in dimensions 4 and higher, we randomly sample 10^4 points uniformly within the domain, with the L_2 error and the relative L_2 error

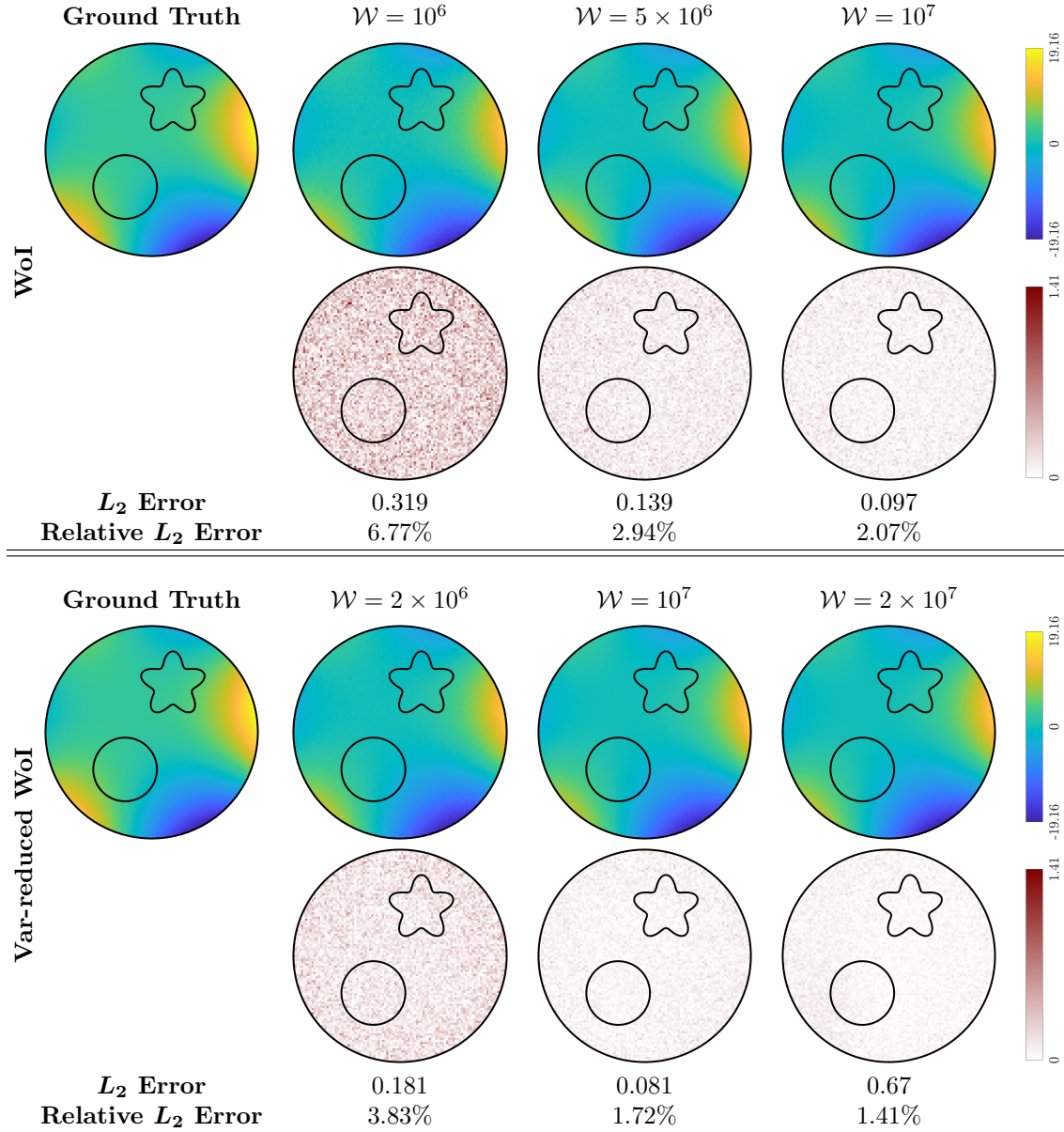


Figure 6: The outer-most circle Ω_1 has $\sigma_1 = 1.5$, Ω_2 is the circle inside with $\sigma_2 = 0.5$, and Ω_3 is the smooth star with $\sigma_3 = 1.1$. In both halves of the figure, the first row shows the solution of WoI or variance-reduced WoI with different numbers of walkers. The second row plots the corresponding errors. The ground truth function is $u(x_1, x_2) = x_1^3 - 3x_1x_2^2$. Both estimators walk $M = 4$ steps.

Table 2: L_2 error and relative L_2 error of estimation of point charge potential placed at the origin of d -dimensional ellipsoidal domains ($d = 3, 4, 5, 6$). Estimator: WoI.

Dim (d)	Walkers (\mathcal{W})	10^6	5×10^6	10^7	2×10^7	3×10^7	4×10^7
3 ($M = 5$)	L_2 Error	0.022	0.020	0.012	0.01062	0.01063	0.01003
	Rel. L_2 Error	2.63%	2.40%	1.44%	1.259%	1.261%	1.19%
4 ($M = 6$)	L_2 Error	0.056	0.033	0.030	0.027	0.028	0.026
	Rel. L_2 Error	7.02%	4.14%	3.81%	3.43%	3.47%	3.30%
5 ($M = 7$)	L_2 Error	0.235	0.122	0.074	0.065	0.061	0.059
	Rel. L_2 Error	25.56%	13.33%	8.05%	7.11%	6.62%	6.39%
6 ($M = 8$)	L_2 Error	0.564	0.244	0.171	0.136	0.162	0.138
	Rel. L_2 Error	56.57%	24.45%	17.20%	13.68%	16.30%	13.91%

reported in Table 2.

Example 3. Continuous Exact Solution with Discontinuity in Gradient.

Because of the piecewise nature of $\sigma(\mathbf{x})$, a common class of solutions to the interface problem consists of C^0 functions whose gradients are discontinuous. However, there are only a few setups for which an explicit analytical formula for such a solution is available.

One such example is provided by Kyle Waller Bower [19], which considers a 2D domain composed of two concentric circles. Let Ω_1 be the outer circle of radius $r_1 = 1$, and Ω_2 be the inner circle of radius $r_2 = \alpha$. Consider the problem such that the solution $u(r, \theta)$ satisfies

$$\left\{ \begin{array}{ll} \Delta u = 0 & \text{on } r \leq 1, r \neq \alpha \\ \partial_{\mathbf{r}} u = \lambda \sin(m\theta) & \text{on } r = 1 \\ [u] = 0 & \text{on } r = \alpha \\ \sigma \partial_{\mathbf{r}^-} u = \partial_{\mathbf{r}^+} u & \text{on } r = \alpha, \end{array} \right. \quad \begin{array}{l} (33a) \\ (33b) \\ (33c) \\ (33d) \end{array}$$

in which $\sigma = \frac{\sigma_2}{\sigma_1}$ is the ratio of $\sigma(\mathbf{x})$ in disks of radius α and 1, and m is a natural

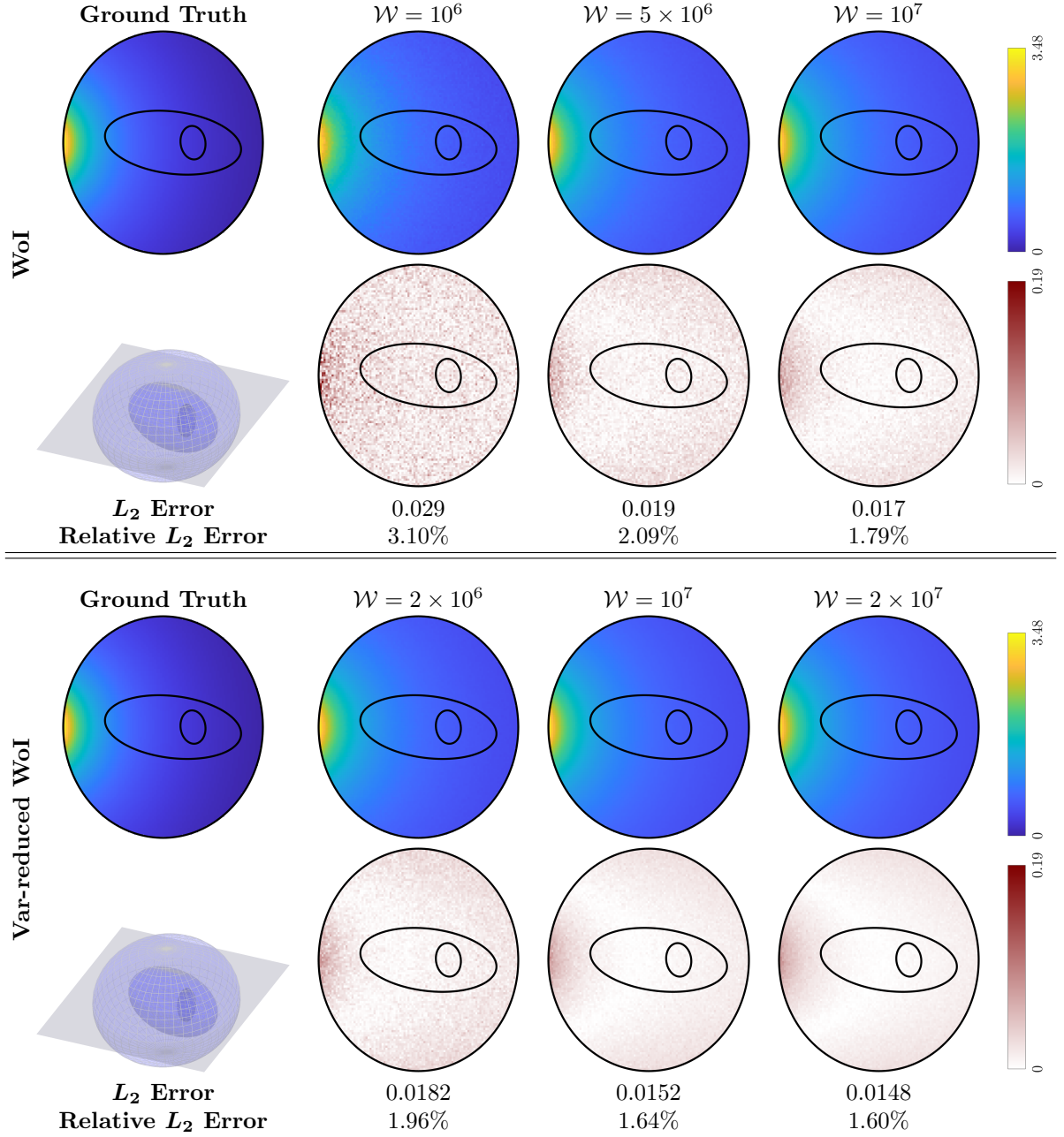


Figure 7: The outer-most ellipsoid Ω_1 with $\sigma_1 = 1.1$, Ω_2 is the middle ellipsoid with $\sigma_2 = 1.3$, and Ω_3 is the inner-most ellipsoid with $\sigma_3 = 0.9$. The first row shows the solution of WoI or variance-reduced WoI with different numbers of walkers. The first figure in the second row shows the domain setup and the equatorial plane. The rest of plots in the second row display corresponding errors. The WoI estimator walks $M = 6$ steps.

number. The analytical solution, obtained by separation of variables on the disk, is

$$u(r, \theta) = \begin{cases} \lambda A r^m \sin(m\theta), & r \leq \alpha \\ \lambda (B r^m + C r^{-m}) \sin(m\theta), & \alpha < r \leq 1 \end{cases}, \quad (34)$$

in which $A = \frac{2}{m} \frac{1}{\alpha^{2m}(\sigma-1)+\sigma+1}$, $B = \frac{A}{2}(\sigma+1)$, and $C = B - \frac{1}{m}$.

We test our methods with $\alpha = 0.4$, $\sigma = \frac{1}{3}$, $m = 3$, and $\lambda = 20$ and present our results in Figure 8.

Andrew Zheng [45] provides yet another example in a domain defined by two concentric spheres. We let Ω_1 be the outer sphere of radius 1, and Ω_2 be the inner sphere of radius α . The problem of interest requires $u(\rho, \theta, \phi)$ to satisfy

$$\begin{cases} \Delta u = 0 & \text{on } r \leq 1, r \neq \alpha \end{cases} \quad (35a)$$

$$\begin{cases} \partial_{\mathbf{r}} u = \lambda \sin(\phi) \cos(\theta) & \text{on } r = 1 \end{cases} \quad (35b)$$

$$\begin{cases} [u] = 0 & \text{on } r = \alpha \end{cases} \quad (35c)$$

$$\begin{cases} \sigma \partial_{\mathbf{r}^-} u = \partial_{\mathbf{r}^+} u & \text{on } r = \alpha, \end{cases} \quad (35d)$$

in which $\theta \in [0, 2\pi)$, $\phi \in [0, \pi)$, $\sigma = \frac{\sigma_2}{\sigma_1}$ is the ratio of $\sigma(\mathbf{x})$ in balls of radius α and 1. By separation of variables again, the analytical solution is

$$u(r, \theta, \phi) = \begin{cases} \lambda A_1^1 r Y_1^1(\theta, \phi), & r \leq \alpha \\ \lambda (B_1^1 r + C_1^1 r^{-2}) Y_1^1(\theta, \phi), & \alpha < r \leq 1 \end{cases}, \quad (36)$$

in which $Y_1^1(\theta, \phi)$ is the spherical harmonics function with $(m, \ell) = (1, 1)$, and A_1^1 , B_1^1 , C_1^1 satisfy the system

$$\begin{bmatrix} 0 & 1 & -2 \\ \alpha & -\alpha & -\alpha^{-2} \\ \sigma & -1 & 2\alpha^{-3} \end{bmatrix} \begin{bmatrix} A_1^1 \\ B_1^1 \\ C_1^1 \end{bmatrix} = \begin{bmatrix} \sqrt{\frac{4\pi}{3}} \\ 0 \\ 0 \end{bmatrix}.$$

In Figure 9, we present the Neumann-to-Dirichlet (NtD) map defined by Eq. (35) by plotting the solution values on the boundary and the interface. Unlike the family of WoS estimators, which typically leave a shell of inaccurate results near the boundary to stop the Brownian motion, and unlike the boundary integral methods that suffer from a near singular kernel when evaluating close-to-interface points, our results demonstrate that our WoI estimators maintain reasonable accuracy on the boundary and across the interfaces.

Convergence. Just like any Monte Carlo estimator, our WoI and variance-reduced WoI estimators have a $\mathcal{O}(1/\sqrt{\mathcal{W}})$ convergence rate, where \mathcal{W} denotes the number of

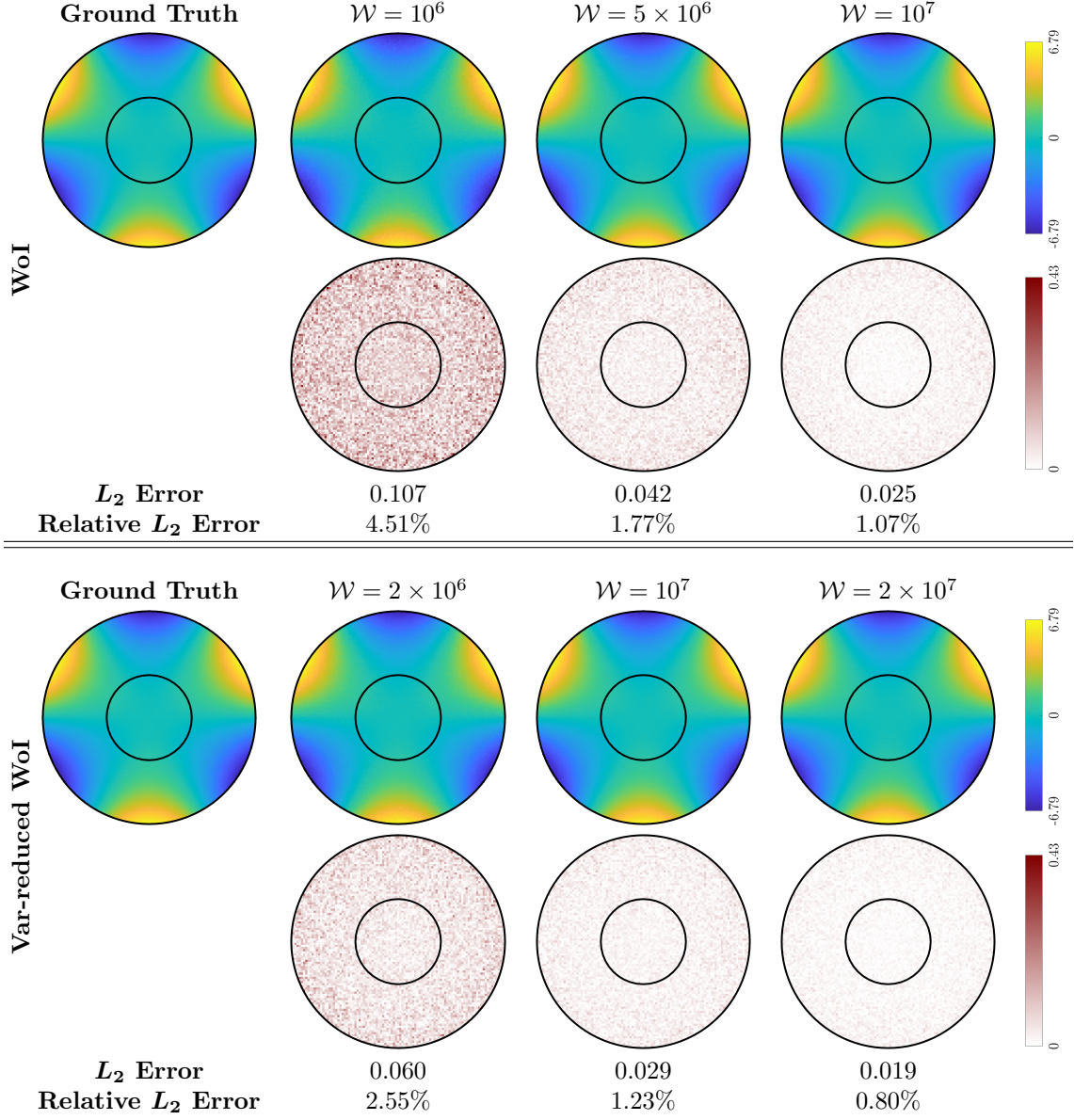


Figure 8: Solution to Eq. (33) with $\alpha = 0.4$, $\sigma = \frac{1}{3}$, $m = 3$, and $\lambda = 20$. In both halves of the figure, the first row shows the solution of WoI or variance-reduced WoI with different numbers of walkers. The second row plots the corresponding errors. Both estimators walk $M = 4$ steps.

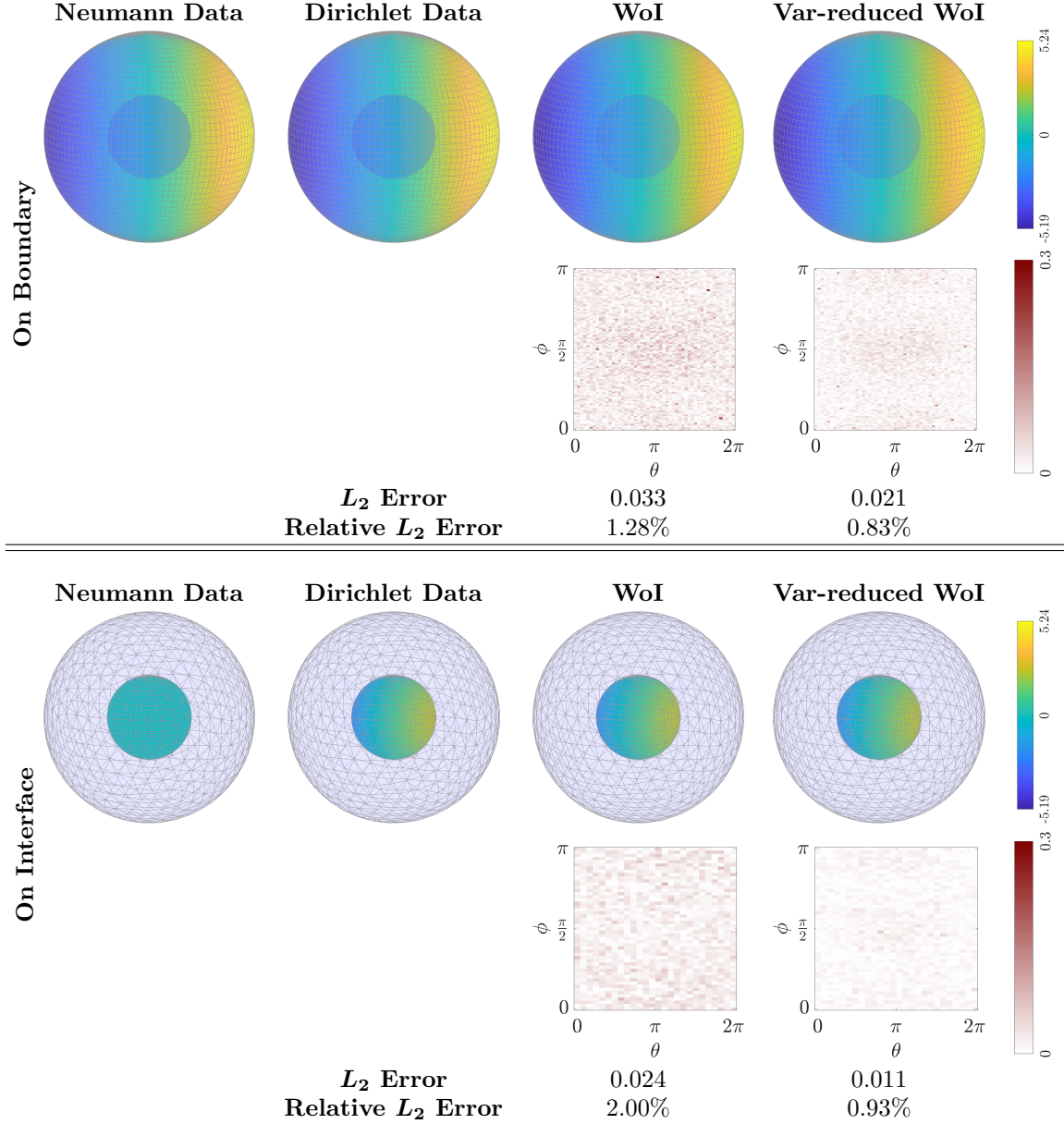


Figure 9: Solution to Eq. (35) with $\alpha = 0.4$, $\sigma = \frac{1}{2}$, and $\lambda = 5$. In both halves of the figure, the first row shows ground truth of the Neumann-to-Dirichlet (NtD) map, the NtD map obtained from WoI with $\mathcal{W} = 10^7$ walkers, and the NtD map obtained from variance-reduced WoI with $\mathcal{W} = 2 \times 10^7$ walkers. The second row plots the corresponding errors in the $\theta - \phi$ parametric space. Both estimators walk $M = 6$ steps. Since the spherical harmonic function Y_1^1 has property $\sin(\phi) \cos(\theta) = \sqrt{\frac{4\pi}{3}} Y_1^1$, the Neumann data on the boundary is proportional to the Dirichlet data.

walkers. The same convergence rate holds for the gradient estimators once boundary and interface query points are excluded. We illustrate the convergence behaviour for the three previous examples in Figure 10. Since the gradient estimators are inaccurate at query points located on the boundary and the interface, we verify the convergence behaviour of the problem defined by Eq. (36) with 7000 randomly sampled query points.

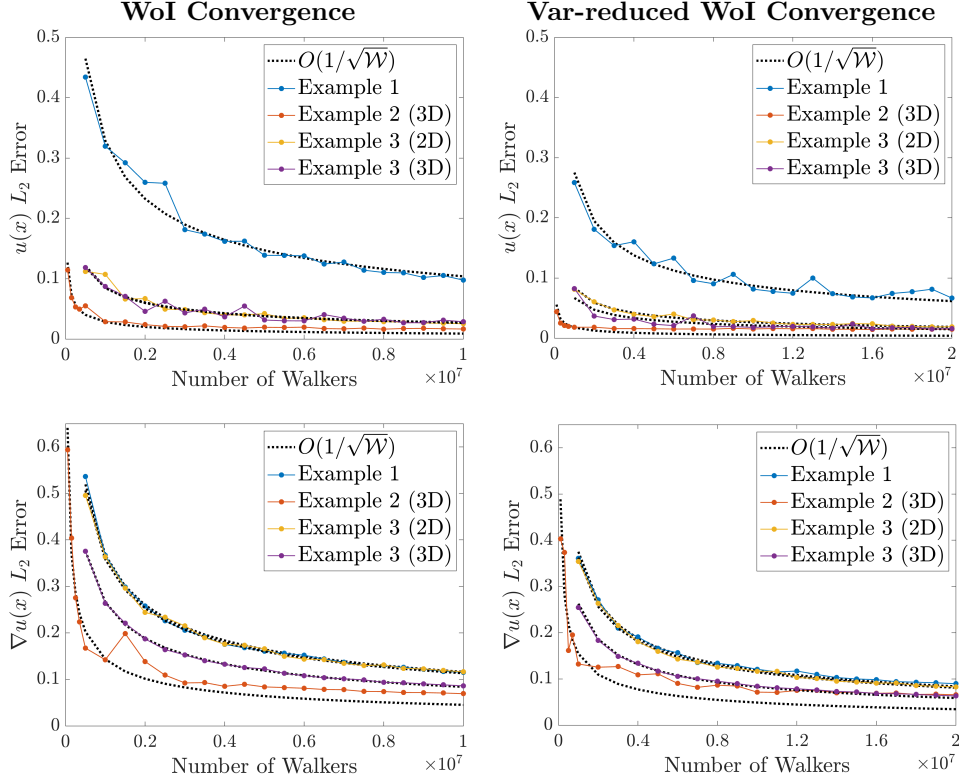


Figure 10: $\mathcal{O}(1/\sqrt{W})$ convergence rate, where W is the number of walkers, of both WoI and variance-reduced WoI estimators and their corresponding gradient estimators. The unexpected tail behavior in the convergence plots for Example 2 (3D) arises because the solution and its gradient are nearly zero over much of the domain, which causes Monte Carlo sampling errors to dominate.

Neural Network Representation. The WoI and variance-reduced WoI estimators have two remaining drawbacks. First, these two Monte Carlo estimators, by design, produce pointwise solutions, which can be restrictive when a continuous form is needed. The error plots presented so far indicate that both the WoI estimator and the variance-reduced WoI estimator exhibit high-frequency errors. However, high-frequency errors are typically considered undesirable artifacts, as the solutions to

many physical systems and real-world problems often exhibit smooth behaviour.

Incorporating a neural network addresses both issues. The universal approximation property of neural networks [17] guarantees a continuous representation of the solution. The neural network learns a coordinate-to-value map, serving as a continuous surrogate for our Monte Carlo estimators, which enables the solution to be evaluated at arbitrary query points without re-running the estimators. In addition, empirical and theoretical studies [29, 2, 4, 9] from the machine learning community point out that deep neural networks exhibit spectral bias, fitting low-frequency components first before other complex components.

Here, we consider a simple multilayer perceptron (MLP) with the *tanh* activation function as the low-pass filter for the errors. Our MLP consists of 6 layers: an input layer whose dimension matches that of the interface problem, four hidden layers of width 64, and a 1-dimensional output layer. We denote the neural network representation of $u(\mathbf{x})$ by $u_\theta(\mathbf{x})$, where θ denotes the trainable parameters. The loss function is defined as the weighted sum of the mean squared errors over the interior and boundary training points,

$$\mathcal{L}(\theta) = \frac{\mu}{\mathcal{N}} \sum_{\mathbf{x} \in \mathcal{X}} |u_\theta(\mathbf{x}) - \hat{u}(\mathbf{x})|^2 + \frac{1}{\mathcal{N}_{\text{bc}}} \sum_{\mathbf{x} \in \mathcal{X}_{\text{bc}}} |\partial_{\mathbf{n}} u_\theta(\mathbf{x}) - b_1(\mathbf{x})|^2, \quad (37)$$

in which \mathcal{X} and \mathcal{X}_{bc} are the sets of training points in Ω and on $\partial\Omega$, respectively, and \mathcal{N} and \mathcal{N}_{bc} are their corresponding cardinalities. The proposed two-term data-driven loss is more straightforward to balance than a PINN-style loss [13, 43] since the number of terms in the latter design scales linearly as the number of interfaces grows. For all our examples, we train the MLP for 15000 epochs using the ADAM optimizer with $\mu = 2$ and a learning rate of 10^{-4} .

Figure 11 and Figure 12 present the learned solutions and learned errors to Eq. (33) and Eq. (35), respectively. For both interface problems, interior training points are sampled on a uniform grid within the circular (or spherical) domain, while boundary training points are uniformly distributed in angular coordinates along the boundary. For Eq. (33), we use $\mathcal{N} = 7845$ points in the domain and $\mathcal{N}_{\text{bc}} = 500$ points on the boundary. For Eq. (35), we use $\mathcal{N} = 8326$ points in the domain and $\mathcal{N}_{\text{bc}} = 5151$ boundary points. The set of test points contains 8000 randomly sampled points within the domain. In both figures, the learned solutions and errors are plotted at the coordinates of the training points. Table 3 reports the L_2 and relative L_2 errors of the learned solutions, using training data generated by WoI and variance-reduced WoI, evaluated on both training and test points.

Before closing this part of the discussion, we note that numerous other neural

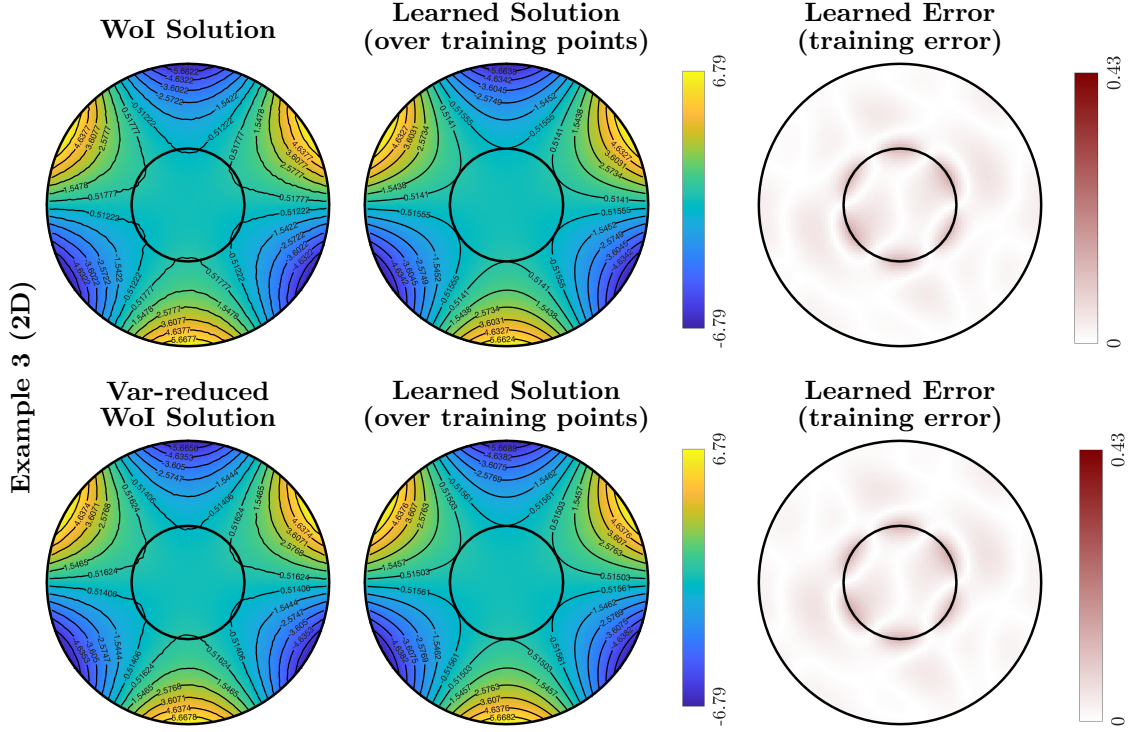


Figure 11: Solution and error of Eq. (34) learned by MLP assumed by the coordinates of training points. The contour lines in both the WoI solution and the variance-reduced WoI solution exhibit noticeable waviness, whereas those in the learned solution are smooth. In contrast to the pixelated error pattern in Figure 8, The error in the learned solution changes smoothly and is concentrated along the interface, where the gradient is C^0 . This error distribution reflects the frequency content present in the ground-truth solution. For consistency, we use the same color scale for errors as in Figure 8 for the purpose of comparing the learned error and the high-frequency Monte Carlo error.

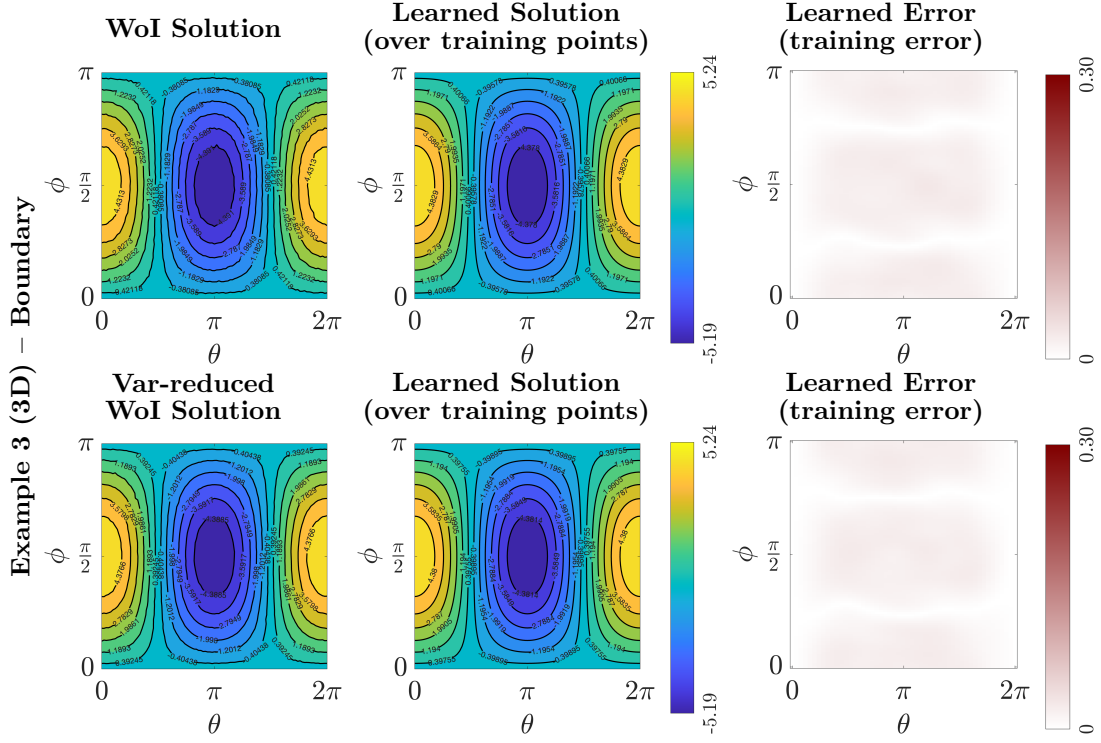


Figure 12: Solution and error of Eq. (36) on the boundary of the domain learned by MLP assumed by the coordinates of training points. The boundary of the spherical domain is presented in $\theta - \phi$ parametric space. The contour lines in both the WoI solution and the variance-reduced WoI solution are wiggly, whereas those in the learned solutions change smoothly. The error in the learned solution change gently comparing with the ones in Figure 9. For consistency, we use the same color scale for error as in Figure 9 for the purpose of comparing the learned error and the high-frequency Monte Carlo error.

Table 3: MLP training and test errors with respect to the true solution. For cases without an analytical ground truth, the numerical solution is used as the reference.

Problem	Data Generator	L_2 Training Error	Relative L_2 Training Error	L_2 Test Error	Relative L_2 Test Error
Ex.3 (2D)	WoI	0.0288	1.21%	0.0289	1.23%
Ex.3 (2D)	Var-reduced WoI	0.029	1.22%	0.029	1.21%
Ex.3 (3D)	WoI	0.015	0.592%	0.022	1.01%
Ex.3 (3D)	Var-reduced WoI	0.015	0.580%	0.021	0.98%
Ex.4	WoI	0.073	3.39%	0.096	3.51%
Ex.4	Var-reduced WoI	0.056	2.64%	0.093	3.41%

network architectures with various activation functions can serve as high-frequency error filters, such as the variant of ResNet [12]. Yet, identifying the optimal neural network design is beyond the scope of this work.

More Applications. Having established the effectiveness of our WoI framework on examples with known ground truth, we now turn to problems rooted in physics and motivated by real-world applications. These problems typically lack analytical solutions, and in some cases, numerical boundary integral solvers fail due to memory constraints. Whenever a numerical solution is available, we compare both the Monte Carlo solution and the learned solution from our framework against it. However, in cases where the boundary integral solver cannot produce a solution, we demonstrate that our framework can still output reasonable and physically meaningful results.

Example 4. The Electrical Conductivity Problem. The electrical conductivity problem models the electrical potential induced by a current in a domain of a conductive medium, given a spatially varying electrical conductivity. The problem serves as the foundational forward problem for a wide range of inverse problems, including Direct Current Resistivity (DCR), Electrical Resistivity Tomography (ERT), and Electrical Impedance Tomography (EIT). We interpret $\sigma(\mathbf{x})$ as the electrical conductivity, $u(\mathbf{x})$ as the electrical potential, and consequently, $-\nabla u(\mathbf{x})$ as the charge density. Since conductivity is an intrinsic material property, it is natural to model $\sigma(\mathbf{x})$ as a piecewise constant function.

We consider a domain with a cow-shaped insulator enclosed by a spherical conductor. Let Ω_1 be the spherical conductor of radius 2 and Ω_2 be the cow interface, where $\sigma_1 = 1.2$ and $\sigma_2 = 0$. The interface problem of interest, described by spherical

coordinates, is

$$\left\{ \begin{array}{ll} \Delta u = 0 & \text{in } \Omega \setminus \partial\Omega_2 \\ \sigma_1 \partial_{\mathbf{r}} u = A \sin^9 \phi \cos^9 \theta & \text{on } \partial\Omega_1 \\ [u](r, \theta, \phi) = 0 & \text{on } \partial\Omega_2 \\ [\sigma \partial_{\mathbf{r}} u](r, \theta, \phi) = 0 & \text{on } \partial\Omega_2, \end{array} \right. \quad \begin{array}{l} (38a) \\ (38b) \\ (38c) \\ (38d) \end{array}$$

in which $\phi \in [0, \pi]$, $\theta \in [0, 2\pi]$, and $A = 10$.

Since Eq. (38) does not admit an analytical solution, we compute a numerical solution using a boundary integral equation method solver developed by Andrew Zheng for comparison [45]. The neural network is trained using $\mathcal{N} = 7200$ random points within the domain and $\mathcal{N}_{bc} = 1000$ points on the boundary. Figure 13 visualizes the domain, a representative slice used to display the solutions, the numerical solution, the WoI and variance-reduced WoI solutions, the learned solutions, and their differences from the numerical solution. Under this setup, the learned solution evaluates the generalization behaviour of the MLP.

Example 5. Groundwater Flow. Groundwater flow through subsurface environments is governed by Darcy's law. In natural settings, the subsurface typically consists of multiple geological materials, such as sand, soil, and rock, each exhibiting distinct hydraulic conductivities. In this context, $u(\mathbf{x})$ represents the hydraulic head, and $\sigma(\mathbf{x})$ denotes the hydraulic conductivity. The model relates the volume flow rate of the fluid, $\sigma(\mathbf{x})\nabla u(\mathbf{x})$, proportionally to the gradient of the hydraulic head and the properties of the porous medium.

We consider a steady-state Darcy flow problem in a hill-shaped domain, where the elevation is higher on the right and lower on the left. Beneath the hill surface are six distinct rocky regions, each characterized by its own hydraulic conductivity. The domain is defined as $\Omega = [-A_1, A_1] \times [-A_2, A_2] \times [-A_3, h(x)]$, in which $h(x)$ describes the hill-shaped upper surface and is defined as

$$h(x) = \begin{cases} kx & \text{if } x \in (-a, a) \\ ka & \text{if } x \in [a, A_1] \\ -ka & \text{if } x \in [-A_1, -a] \end{cases}.$$

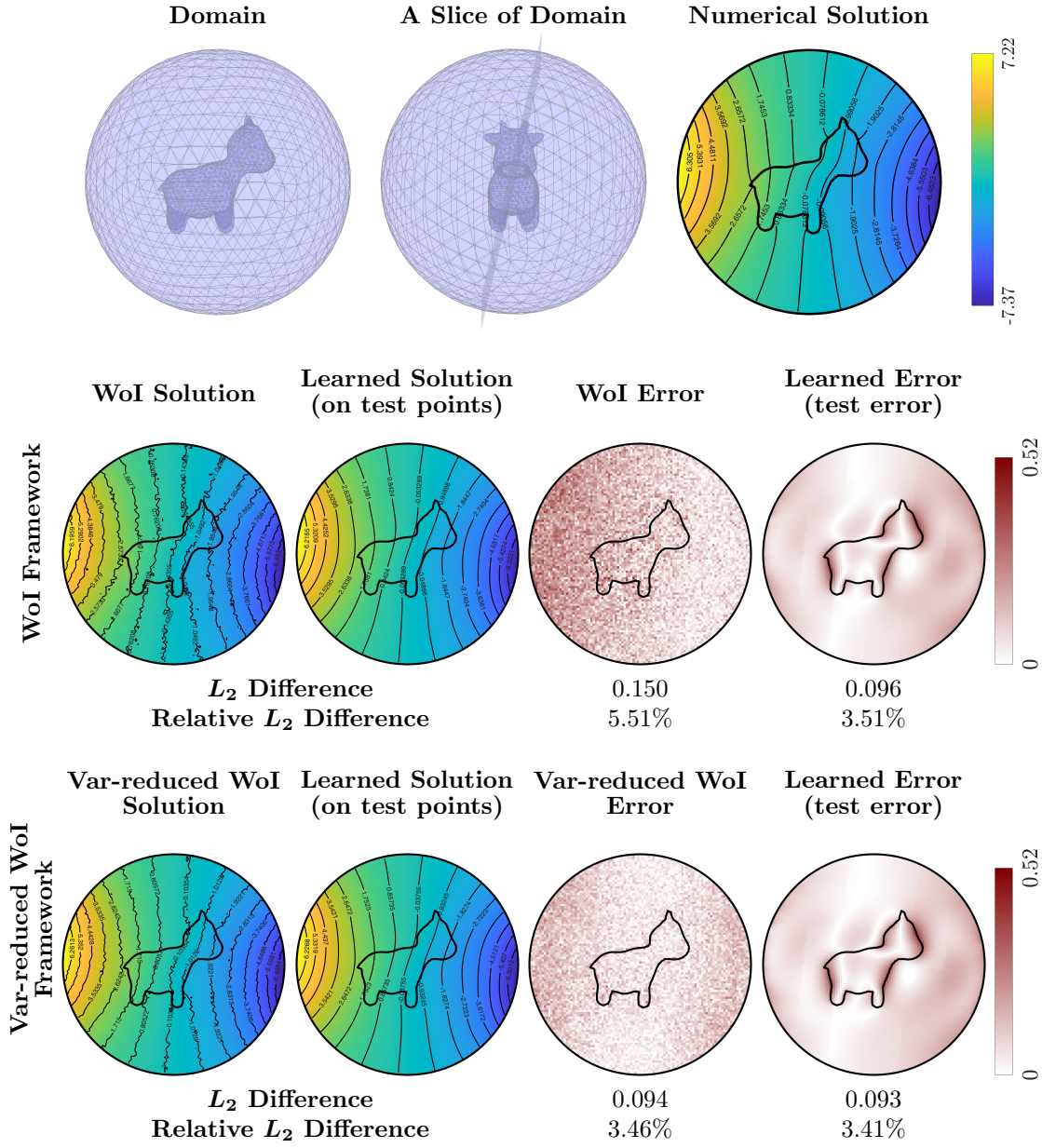


Figure 13: The first row shows the domain, a slice of the domain we show our estimation on, and the numerical solution obtained by a boundary integral equation method solver [45]. The second row shows the solution and error estimated by WoI, and the learned solution and error with training data generated by the WoI estimator. The third row shows the solution and error estimated by variance-reduced WoI, and the learned solution and error with training data generated by the variance-reduced WoI estimator.

The hydraulic head satisfies the interface problem,

$$\left\{ \begin{array}{l} \Delta u = 0 \quad \text{in } \Omega \setminus \bigcup_{i=2}^7 \partial\Omega_i \\ \sigma_1 \partial_{\mathbf{n}} u = \begin{cases} \sin(\pi x/A_1) \cos(\pi y/2A_1) & \text{if } z = h(x) \\ 0 & \text{otherwise} \end{cases} \quad \text{on } \partial\Omega_1, \\ [u](\mathbf{x}) = 0 \quad \text{on } \partial\Omega_i, \forall i \in \{2, 3, 4, 5, 6, 7\} \\ [\sigma \partial_{\mathbf{n}} u](\mathbf{x}) = 0 \quad \text{on } \partial\Omega_i, \forall i \in \{2, 3, 4, 5, 6, 7\} \end{array} \right. \quad \begin{array}{l} (39a) \\ (39b) \\ (39c) \\ (39d) \end{array}$$

that enforces continuity of head across material boundaries. The boundary conditions are interpreted as representing rainfall on the hilltop and water extraction in a residential area located downhill.

We solve Eq. (39) with $A_1 = A_3 = 2$, $A_2 = 1.5$, $a = 1.2$ and $k = \frac{1}{3}$. While the numerical solver [45] fails to produce a solution due to the number of interfaces, our framework successfully computes a descent solution. We present our WoI solution, variance-reduced WoI solution, and learned solutions over a slice of the domain in Figure 14. The neural network is trained using $\mathcal{N} = 7200$ randomly sampled in the domain and $\mathcal{N}_{\text{bc}} = 1200$ points on the boundary. The learned solution is, therefore, assumed by a separate set of test points.

6 Conclusion

Herein presented was a grid-free, highly parallelizable Monte Carlo estimator, WoI, that has $\mathcal{O}(1/\sqrt{\mathcal{W}})$ convergence rate for solving an elliptic interface problem. We demonstrated that our estimator has uniform accuracy up to the boundary, close to the interfaces, and in the interior of the domain in contrast to other methods for this problem. Moreover, the estimator generalizes naturally to higher dimensional problems that are intractable to grid-based methods. Also, we can readily compute the gradient of the solution with almost no extra computational cost. Finally, we introduced the WoI framework in which our Monte Carlo estimator acts as a data generator for training a neural network.

Several promising directions remain open for future research. While we have proposed one effective PDF in Eq. (17) and Eq. (18), alternative PDFs that consider the geometric properties of the boundary and the interfaces may lead to improved efficiency or accuracy. Also, it would be interesting to explore whether and how our Monte Carlo estimator can be extended to other boundary conditions, such as

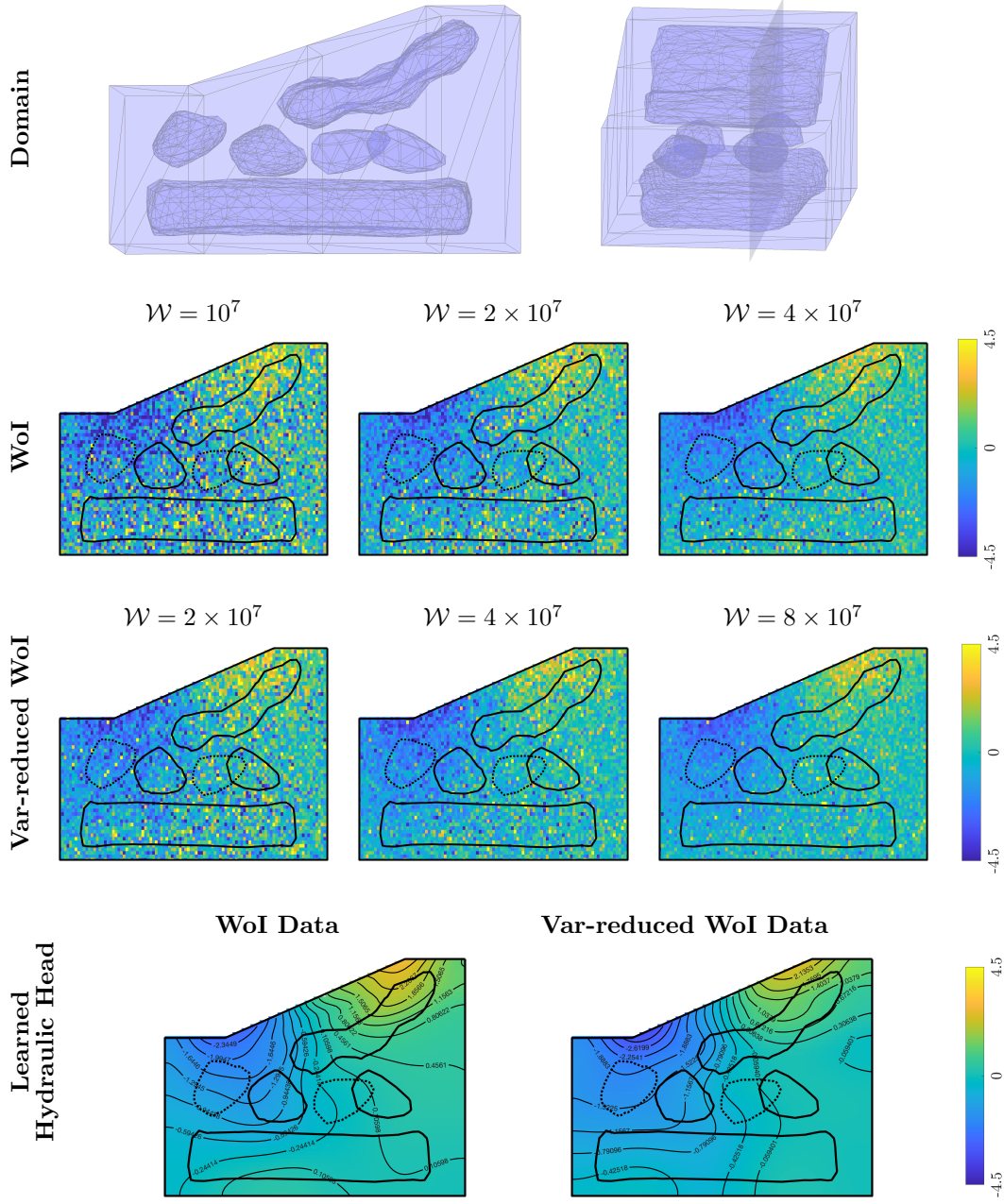


Figure 14: WoI and variance-reduced WoI solution to Eq. (39) and learned solution using data generated by both Monte Carlo methods. Both estimators walk $N = 5$ steps. The rocks with dotted outline do not intersect with the cutting plane. The hill is Ω_1 , the tilted rock at top is Ω_2 , the four rocks in the middle are $\Omega_3, \Omega_4, \Omega_5, \Omega_6$, the bedrock at the bottom is Ω_7 . We set $\sigma_1 = 0.2$, $\sigma_2 = 0.05$, $\sigma_3 = \sigma_4 = \sigma_5 = \sigma_6 = 0.03$, $\sigma_7 = 0.005$ with unit cm/s.

Dirichlet, Robin, or mixed. Similarly, seeking the possibility of adapting our estimator to more general elliptic PDEs that include advection and reaction terms is another compelling direction for future research. Study of the network architectures that can represent solutions to these elliptic interface problems and be effectively trained by WoI data are of particular importance. Recent work [24] has introduced a neural field construction capable of representing continuous functions with discontinuous gradients. Integrating such representation into our framework may improve the accuracy of the learned solutions.

Acknowledgments

We express our gratitude to Andrew Zheng for his contribution in generating the numerical solution in Example 4. We also thank the Mathcha team for providing an excellent platform that facilitated the creation of our diagrams. Additionally, we acknowledge the authors of gptoolbox and the MATLAB tree structure for their toolboxes, which helped us build some of our code.

References

- [1] Alex H. Barnett, Gary R. Marple, Shravan Veerapaneni, and Lin Zhao. A unified integral equation scheme for doubly periodic Laplace and Stokes boundary value problems in two dimensions. *Communications on Pure and Applied Mathematics*, 71(11):2334–2380, 2018.
- [2] Alberto Bietti and Julien Mairal. On the inductive bias of neural tangent kernels. In H. Wallach, H. Larochelle, A. Beygelzimer, F. d'Alché-Buc, E. Fox, and R. Garnett, editors, *Advances in Neural Information Processing Systems*, volume 32. Curran Associates, Inc., 2019.
- [3] Mireille Bossy, Nicolas Champagnat, Sylvain Maire, and Denis Talay. Probabilistic interpretation and random walk on spheres algorithms for the Poisson-Boltzmann equation in molecular dynamics. *ESAIM: Mathematical Modelling and Numerical Analysis*, 44(5):997–1048, 2010.
- [4] Yuan Cao, Zhiying Fang, Yue Wu, Ding-Xuan Zhou, and Quanquan Gu. Towards understanding the spectral bias of deep learning. In Zhi-Hua Zhou, editor, *Proceedings of the Thirtieth International Joint Conference on Artificial Intelli-*

- gence, *IJCAI-21*, pages 2205–2211. International Joint Conferences on Artificial Intelligence Organization, 8 2021. Main Track.
- [5] J.C. de Munck, T.J.C. Faes, and R.M. Heethaar. The boundary element method in the forward and inverse problem of electrical impedance tomography. *IEEE Transactions on Biomedical Engineering*, 47(6):792–800, 2000.
 - [6] G. Dong, J. Zou, R. H. Bayford, X. Ma, S. Gao, W. Yan, and M. Ge. The comparison between FVM and FEM for EIT forward problem. *IEEE Transactions on Magnetics*, 41(5):1468–1471, 2005.
 - [7] W. D. Evans. Partial Differential Equations. *Bulletin of the London Mathematical Society*, 20(4):375–376, 1988.
 - [8] Qiwei Feng, Bin Han, and Peter Minev. Sixth-order hybrid finite difference methods for elliptic interface problems with mixed boundary conditions. *Journal of Computational Physics*, 497:112635, 2024.
 - [9] Sara Fridovich-Keil, Raphael Gontijo-Lopes, and Rebecca Roelofs. Spectral bias in practice: the role of function frequency in generalization. In *Proceedings of the 36th International Conference on Neural Information Processing Systems*, NIPS ’22, Red Hook, NY, USA, 2022. Curran Associates Inc.
 - [10] L. Greengard and V. Rokhlin. A fast algorithm for particle simulations. *Journal of Computational Physics*, 73(2):325–348, 1987.
 - [11] Ruchi Guo and Tao Lin. An immersed finite element method for elliptic interface problems in three dimensions. *Journal of Computational Physics*, 414:109478, 2020.
 - [12] Jihun Han, Mihai Nica, and Adam R. Stinchcombe. A derivative-free method for solving elliptic partial differential equations with deep neural networks. *Journal of Computational Physics*, 419:109672, 2020.
 - [13] Cuiyu He, Xiaozhe Hu, and Lin Mu. A mesh-free method using piecewise deep neural network for elliptic interface problems. *Journal of Computational and Applied Mathematics*, 412:114358, 2022.
 - [14] Johan Helsing and Rikard Ojala. On the evaluation of layer potentials close to their sources. *Journal of Computational Physics*, 227(5):2899–2921, 2008.
 - [15] Kenneth L Ho. *Fast direct methods for molecular electrostatics*. New York University, 2012.

- [16] Andreas Klöckner, Alexander Barnett, Leslie Greengard, and Michael O’Neil. Quadrature by expansion: A new method for the evaluation of layer potentials. *Journal of Computational Physics*, 252:332–349, 2013.
- [17] Anastasis Kratsios. The universal approximation property: Characterization, construction, representation, and existence. *Annals of Mathematics and Artificial Intelligence*, 89:435–469, 2021. Published 22 January 2021.
- [18] Rainer Kress. *Linear integral equations*. Springer, 2014.
- [19] Kyle Waller Bower. *The Electrostatic Problem for Piecewise Constant Conductivities in Two Dimensions: Numerical Methods and Optimal Regularity*. Phd thesis, University of Toronto, 2024.
- [20] Andreas E. Kyprianou, Ana Osojnik, and Tony Shardlow. Unbiased ‘walk-on-spheres’ Monte Carlo methods for the fractional Laplacian. *IMA Journal of Numerical Analysis*, 38(3):1550–1578, August 2017.
- [21] Auguste De Lambilly, Gabriel Benedetti, Nour Rizk, Chen Hanqi, Siyuan Huang, Junnan Qiu, David Louapre, Raphael Granier De Cassagnac, and Damien Rohmer. Heat simulation on meshless crafted-made shapes. In *Proceedings of the 16th ACM SIGGRAPH Conference on Motion, Interaction and Games (MIG ’23)*, pages 1–7, New York, NY, USA, 2023. Association for Computing Machinery.
- [22] Randall J. LeVeque and Zhilin Li. The immersed interface method for elliptic equations with discontinuous coefficients and singular sources. *SIAM Journal on Numerical Analysis*, 31(4):1019–1044, 1994.
- [23] Zhilin Li. A fast iterative algorithm for elliptic interface problems. *SIAM Journal on Numerical Analysis*, 35(1):230–254, 1998.
- [24] Mengfei Liu, Yue Chang, Zhecheng Wang, Peter Yichen Chen, and Eitan Grinspun. Precise gradient discontinuities in neural fields for subspace physics, 2025.
- [25] P.-G. Martinsson. *Fast Direct Solvers for Elliptic PDEs*. CBMS-NSF Regional Conference Series in Applied Mathematics. Society for Industrial and Applied Mathematics, Philadelphia, PA, 2019.
- [26] Bailey Miller, Rohan Sawhney, Keenan Crane, and Ioannis Gkioulekas. Walkin’ Robin: Walk on stars with Robin boundary conditions. *ACM Trans. Graph.*, 43(4), jul 2024.

- [27] Mervin E. Muller. Some continuous Monte Carlo methods for the Dirichlet problem. *The Annals of Mathematical Statistics*, 27(3):569–589, September 1956.
- [28] J R Philip. Flow in porous media. *Annual Review of Fluid Mechanics*, 2(Volume 2, 1970):177–204, 1970.
- [29] Nasim Rahaman, Aristide Baratin, Devansh Arpit, Felix Draxler, Min Lin, Fred Hamprecht, Yoshua Bengio, and Aaron Courville. On the spectral bias of neural networks. In Kamalika Chaudhuri and Ruslan Salakhutdinov, editors, *Proceedings of the 36th International Conference on Machine Learning*, volume 97 of *Proceedings of Machine Learning Research*, pages 5301–5310. PMLR, 09–15 Jun 2019.
- [30] Karl K. Sabelfeld. Vector algorithms in the Monte-Carlo method for solving systems of second-order elliptic equations and Lamé’s equation. *Doklady Akademii Nauk SSSR*, 262(5):1076–1080, 1982. In Russian.
- [31] Karl K. Sabelfeld. *Monte Carlo Methods in Boundary Value Problems*. Springer, Berlin, Heidelberg, 1991.
- [32] Karl K. Sabelfeld and N. A. Simonov. *Stochastic methods for boundary value problems: Numerics for high-dimensional PDEs and applications*. De Gruyter, 2016.
- [33] Karl K. Sabelfeld and Nikolai A. Simonov. *Random Walks on Boundary for Solving PDEs*. De Gruyter, Berlin, 1994.
- [34] Daya Sagar, Qiuming Cheng, and Frits Agterberg. *Handbook of mathematical geosciences: fifty years of IAMG*. Springer Nature, 2018.
- [35] Rohan Sawhney, Bailey Miller, Ioannis Gkioulekas, and Keenan Crane. Walk on stars: A grid-free Monte Carlo method for PDEs with neumann boundary conditions. *ACM Trans. Graph.*, 2023.
- [36] Rohan Sawhney, Dario Seyb, Wojciech Jarosz, and Keenan Crane. Grid-free Monte Carlo for PDEs with spatially varying coefficients. *ACM Transactions on Graphics (Proceedings of SIGGRAPH)*, 41(4), July 2022.
- [37] Marek Stastna, Andrew P. Grace, and Travis Robinson. Exact solutions for flow through porous media with the klinkenberg effect. *AIP Advances*, 13(1):015309, 01 2023.

- [38] Ryusuke Sugimoto, Terry Chen, Yiti Jiang, Christopher Batty, and Toshiya Hachisuka. A practical walk-on-boundary method for boundary value problems. *ACM Trans. Graph.*, 42(4), jul 2023.
- [39] Renato S. Tavares, Flávio A. Nakadaira Filho, Marcos S.G. Tsuzuki, Thiago C. Martins, and Raul Gonzalez Lima. Discretization error and the EIT forward problem. *IFAC Proceedings Volumes*, 47(3):7535–7540, 2014. 19th IFAC World Congress.
- [40] Teemu Tyni, Adam R. Stinchcombe, and Spyros Alexakis. A boundary integral equation method for the complete electrode model in electrical impedance tomography with tests on experimental data. *SIAM Journal on Imaging Sciences*, 17(1):672–705, 2024.
- [41] Sylvain Vallaghé and Théodore Papadopoulos. A trilinear immersed finite element method for solving the electroencephalography forward problem. *SIAM Journal on Scientific Computing*, 32(4):2379–2394, 2010.
- [42] Liqun Wang, Hui Zheng, Xin Lu, and Liwei Shi. A Petrov-Galerkin finite element interface method for interface problems with Bloch-periodic boundary conditions and its application in phononic crystals. *Journal of Computational Physics*, 393:117–138, 2019.
- [43] Sidi Wu, Aiqing Zhu, Yifa Tang, and Benzhuo Lu. Solving parametric elliptic interface problems via interfaced operator network. *Journal of Computational Physics*, 514:113217, 2024.
- [44] Wenjun Ying and J. Thomas Beale. A fast accurate boundary integral method for potentials on closely packed cells. *Communications in Computational Physics*, 14(4):1073–1093, 2013.
- [45] Andrew Zheng. Boundary element method for the 3D electric impedance tomography forward problem. Master’s thesis, University of Toronto, 2024.

A A Proof of Theorem 4.1

We prove Theorem 4.1 in this appendix.

Theorem A.1. *Given a query point \mathbf{x} and a fixed set of $h_0, h_1, \dots, h_i \in \{1, \dots, N\}$. Let $\{Y_0, Y_1, \dots, Y_i, \dots\}$ be a Markov chain starting from \mathbf{x} such that $Y_i \in \partial\Omega_{h_i}$.*

Let $p_0(\mathbf{x}, \mathbf{y})$ and $p(\mathbf{x}, \mathbf{y})$ be any probability density functions (PDFs) denoting the transitional distribution of \mathbf{y} given \mathbf{x} . Define a family of functions

$$Q_{(h_i, \dots, h_1, h_0)}^* = \begin{cases} \frac{\beta_{h_0}(Y_0)}{p_0(\mathbf{x}, Y_0)} & \text{if } i = 0 \\ Q_{(h_{i-1}, \dots, h_1, h_0)}^* \frac{K_{h_i, h_{i-1}}^*(Y_i, Y_{i-1})}{p(Y_{i-1}, Y_i)} & \text{if } i \geq 1. \end{cases} \quad (40)$$

Then, $Q_{(h_i, \dots, h_1, h_0)}^* \Phi(\mathbf{x}, Y_i)$ is an unbiased estimator for

$$\int_{\partial\Omega_{h_i}} \Phi(\mathbf{x}, \mathbf{y}) (\mathcal{K}_{h_i, h_{i-1}}^* \cdots \mathcal{K}_{h_2, h_1}^* \mathcal{K}_{h_1, h_0}^* \beta_{h_0}) dA_{\mathbf{y}}.$$

i.e.

$$\int_{\partial\Omega_{h_i}} \Phi(\mathbf{x}, \mathbf{y}) (\mathcal{K}_{h_i, h_{i-1}}^* \cdots \mathcal{K}_{h_2, h_1}^* \mathcal{K}_{h_1, h_0}^* \beta_{h_0}) dA_{\mathbf{y}} = \mathbb{E} \left[Q_{(h_i, \dots, h_1, h_0)}^* \Phi(\mathbf{x}, Y_i) \right].$$

Proof. Unwrapping the recursive definition of $Q_{(h_i, \dots, h_1, h_0)}^*$, we have

$$Q_{(h_i, \dots, h_1, h_0)}^* = \frac{\prod_{m=1}^i K_{h_m, h_{m-1}}^*(Y_m, Y_{m-1})}{\prod_{m=1}^i p(Y_{m-1}, Y_m)} \frac{\beta_{h_0}(Y_0)}{p_0(\mathbf{x}, Y_0)}$$

Let $\rho_{Y_0, Y_1, \dots, Y_i}(\mathbf{y}_0, \mathbf{y}_1, \dots, \mathbf{y}_i)$ be the joint distribution of Y_0, Y_1, \dots, Y_i . By chain rule,

$$\begin{aligned} \rho_{Y_0, Y_1, \dots, Y_i}(\mathbf{y}_0, \mathbf{y}_1, \dots, \mathbf{y}_i) &= p_0(\mathbf{x}, \mathbf{y}_0) \mathbb{P}(\mathbf{y}_1 | \mathbf{y}_0) \mathbb{P}(\mathbf{y}_2 | \mathbf{y}_0, \mathbf{y}_1) \cdots \mathbb{P}(\mathbf{y}_i | \mathbf{y}_0, \mathbf{y}_1, \dots, \mathbf{y}_{i-1}) \\ &= p_0(\mathbf{x}, \mathbf{y}_0) \mathbb{P}(\mathbf{y}_1 | \mathbf{y}_0) \mathbb{P}(\mathbf{y}_2 | \mathbf{y}_1) \cdots \mathbb{P}(\mathbf{y}_i | \mathbf{y}_{i-1}) \\ &= p_0(\mathbf{x}, \mathbf{y}_0) p(\mathbf{y}_0, \mathbf{y}_1) p(\mathbf{y}_1, \mathbf{y}_2) \cdots p(\mathbf{y}_{i-1}, \mathbf{y}_i) \\ &= p_0(\mathbf{x}, \mathbf{y}_0) \prod_{m=1}^i p(\mathbf{y}_{m-1}, \mathbf{y}_m), \end{aligned}$$

where the second equality holds since $Y_0, Y_1, \dots, Y_i, \dots$ is a Markov chain, and the third equality follows immediately from the definition of transitional probability, $p(\mathbf{x}, \mathbf{y}) = \mathbb{P}(\mathbf{y} | \mathbf{x})$. By definition of expected value,

$$\begin{aligned} &\mathbb{E} \left[Q_{(h_i, \dots, h_1, h_0)}^* \Phi(\mathbf{x}, Y_i) \right] \\ &= \int_{\partial\Omega_{h_i}} \cdots \int_{\partial\Omega_{h_1}} \int_{\partial\Omega_{h_0}} Q_{(h_i, \dots, h_1, h_0)}^* \Phi(\mathbf{x}, \mathbf{y}_i) \rho_{Y_0, Y_1, \dots, Y_i}(\mathbf{y}_0, \mathbf{y}_1, \dots, \mathbf{y}_i) d\ell_{\mathbf{y}_{h_0}} d\ell_{\mathbf{y}_{h_1}} \cdots d\ell_{\mathbf{y}_{h_i}}. \end{aligned} \quad (41)$$

Substitute $Q_{(h_i, \dots, h_1, h_0)}^*$ and $\rho_{Y_0, Y_1, \dots, Y_i}(\mathbf{y}_0, \mathbf{y}_1, \dots, \mathbf{y}_i)$, then we have

$$\begin{aligned}
& \mathbb{E} \left[Q_{(h_i, \dots, h_1, h_0)}^* \Phi(\mathbf{x}, Y_i) \right] \\
&= \int_{\partial\Omega_{h_i}} \cdots \int_{\partial\Omega_{h_1}} \int_{\partial\Omega_{h_0}} \frac{\prod_{m=1}^i K_{h_m, h_{m-1}}^*(\mathbf{y}_m, \mathbf{y}_{m-1})}{\prod_{m=1}^i p(\mathbf{y}_{m-1}, \mathbf{y}_m)} \frac{\beta_{h_0}(\mathbf{y}_0)}{p_0(\mathbf{x}, \mathbf{y}_0)} \Phi(\mathbf{x}, \mathbf{y}_i) \\
&\quad p_0(\mathbf{x}, \mathbf{y}_0) \prod_{m=1}^i p(\mathbf{y}_{m-1}, \mathbf{y}_m) d\ell_{\mathbf{y}_{h_0}} d\ell_{\mathbf{y}_{h_1}} \cdots d\ell_{\mathbf{y}_{h_i}} \\
&= \int_{\partial\Omega_{h_i}} \cdots \int_{\partial\Omega_{h_1}} \int_{\partial\Omega_{h_0}} \prod_{m=1}^i K_{h_m, h_{m-1}}^*(\mathbf{y}_m, \mathbf{y}_{m-1}) \beta_{h_0}(\mathbf{y}_0) \Phi(\mathbf{x}, \mathbf{y}_i) d\ell_{\mathbf{y}_{h_0}} d\ell_{\mathbf{y}_{h_1}} \cdots d\ell_{\mathbf{y}_{h_i}} \\
&= \int_{\partial\Omega_{h_i}} \Phi(\mathbf{x}, \mathbf{y}) (\mathcal{K}_{h_i, h_{i-1}}^* \cdots \mathcal{K}_{h_2, h_1}^* \mathcal{K}_{h_1, h_0}^* \beta_{h_0}) d\ell_{\mathbf{y}},
\end{aligned}$$

as required. \square

B A Proof of Theorem 4.2

We prove Theorem 4.2 in this appendix.

Theorem B.1. *Let H_0, H_1, \dots, H_i be independent discrete random variables with p.d.f*

$$\mathbb{P}(H_i = n) = \begin{cases} \frac{1}{N} & \forall n \in \{1, \dots, N\}, \text{ when } i = 0 \\ \frac{|\alpha_n|}{\|\alpha\|_1} & \forall n \in \{1, \dots, N\}, \text{ when } i \geq 1 \end{cases},$$

where $\|\cdot\|_1$ is the ℓ_1 norm. It can be shown that

$$\begin{aligned}
& \sum_{h_i, \dots, h_1, h_0=1}^N \int_{\partial\Omega_{h_i}} \Phi(\mathbf{x}, \mathbf{y}) \left((\alpha_{h_i} \mathcal{K}_{h_i, h_{i-1}}^*) \cdots (\alpha_{h_2} \mathcal{K}_{h_2, h_1}^*) (\alpha_{h_1} \mathcal{K}_{h_1, h_0}^*) \beta_{h_0} \right) d\ell_{\mathbf{y}} \\
&= N \|\alpha\|_1^i \mathbb{E}_{H_i, \dots, H_0} \left[\prod_{m=1}^i \text{sign}(\alpha_{H_m}) \int_{\partial\Omega_{H_i}} \Phi(\mathbf{x}, \mathbf{y}) \left(\mathcal{K}_{H_i, H_{i-1}}^* \cdots \mathcal{K}_{H_1, H_0}^* \beta_{H_0} d\ell_{\mathbf{y}} \right) \right].
\end{aligned}$$

Proof. Since H_0, H_1, \dots, H_M are independent, their joint probability density is

$$\begin{aligned}
\mathbb{P}(H_0 = h_0, H_1 = h_1, \dots, H_i = h_i) &= \mathbb{P}(H_0 = h_0) \left(\prod_{m=1}^i \mathbb{P}(H_i = h_i) \right) \\
&= \frac{1}{N} \left(\prod_{m=1}^i \frac{|\alpha_{h_m}|}{\|\alpha\|_1} \right).
\end{aligned}$$

Observe that $\alpha_{h_i} = \text{sign}(\alpha_{h_i})|\alpha_{h_i}|$ holds for all $h_i \in \{1, \dots, N\}$. Then,

$$\begin{aligned}
& \sum_{h_i, \dots, h_1, h_0=1}^N \int_{\partial\Omega_{h_i}} \Phi(\mathbf{x}, \mathbf{y}) \left((\alpha_{h_i} \mathcal{K}_{h_i, h_{i-1}}^*) \cdots (\alpha_{h_2} \mathcal{K}_{h_2, h_1}^*) (\alpha_{h_1} \mathcal{K}_{h_1, h_0}^*) \beta_{h_0} \right) d\ell_{\mathbf{y}} \\
&= \sum_{h_i, \dots, h_1, h_0=1}^N \left(\prod_{m=1}^i \text{sign}(\alpha_{h_m}) |\alpha_{h_m}| \right) \int_{\partial\Omega_{h_i}} \Phi(\mathbf{x}, \mathbf{y}) (\mathcal{K}_{h_i, h_{i-1}}^* \cdots \mathcal{K}_{h_2, h_1}^* \mathcal{K}_{h_1, h_0}^* \beta_{h_0}) d\ell_{\mathbf{y}} \\
&= N \|\alpha\|^i \sum_{h_i, \dots, h_1, h_0=1}^N \left(\frac{1}{N} \prod_{m=1}^i \frac{|\alpha_{h_m}|}{\|\alpha\|} \right) \left(\prod_{m=1}^i \text{sign}(\alpha_{h_m}) \right) \\
&\quad \int_{\partial\Omega_{h_i}} \Phi(\mathbf{x}, \mathbf{y}) (\mathcal{K}_{h_i, h_{i-1}}^* \cdots \mathcal{K}_{h_2, h_1}^* \mathcal{K}_{h_1, h_0}^* \beta_{h_0}) d\ell_{\mathbf{y}} \\
&= N \|\alpha\|^i \sum_{h_i, \dots, h_1, h_0=1}^N \mathbb{P}(H_0 = h_0, H_1 = h_1, \dots, H_i = h_i) \left(\prod_{m=1}^i \text{sign}(\alpha_{h_m}) \right) \\
&\quad \int_{\partial\Omega_{h_i}} \Phi(\mathbf{x}, \mathbf{y}) (\mathcal{K}_{h_i, h_{i-1}}^* \cdots \mathcal{K}_{h_2, h_1}^* \mathcal{K}_{h_1, h_0}^* \beta_{h_0}) d\ell_{\mathbf{y}} \\
&= N \|\alpha\|_1^i \mathbb{E}_{H_i, \dots, H_0} \left[\prod_{m=1}^i \text{sign}(\alpha_{H_m}) \int_{\partial\Omega_{H_i}} \Phi(\mathbf{x}, \mathbf{y}) \left(\mathcal{K}_{H_i, H_{i-1}}^* \cdots \mathcal{K}_{H_1, H_0}^* \beta_{H_0} d\ell_{\mathbf{y}} \right) \right],
\end{aligned}$$

where the last step follows immediately from the definition of the expected value.